Available online at www.sciencedirect.com
SCIENCE DIRECT®
Journal of the Mechanics and Physics of Solids
54 (2006) 1276–1303
JOURNAL OF THE MECHANICS AND PHYSICS OF SOLIDS
www.elsevier.com/locate/jmps

Quantum mechanics based multiscale modeling of stress-induced phase transformations in iron

A. Lew[a], K. Caspersen[b], E.A. Carter[b], M. Ortiz[c,*]

[a]*Mechanical Engineering, Stanford University, Stanford, CA 94305-4040, USA*
[b]*Department of Mechanical and Aerospace Engineering and Program in Applied and Computational Mathematics, Princeton University, Princeton, NJ 08544-5263, USA*
[c]*GALCIT, California Institute of Technology, Pasadena, CA 91125, USA*

Received 15 August 2005; received in revised form 3 November 2005; accepted 19 November 2005

Abstract

The ground state crystal structure of Fe, ferromagnetic body-centered cubic (bcc), undergoes a stress-induced martensitic phase transformation to a hexagonally close-packed (hcp) structure. Both bcc and hcp have been observed to coexist over a large range deformations, such that the nonlinearities in the constitutive behavior of *each phase* need to be included for an accurate description. We present herein a methodology to construct high-fidelity quantum mechanics based nonlinear elastic energy densities, amenable to be included in microstructural optimization procedures like sequential lamination. We use the model to show that the transition pressure (TP) has a strong dependence on relatively small amounts of shear deformation, and to investigate the value of the TP under uniaxial compressions, presumably found in shock-loaded materials. Results hint that more complex deformation patterns may need be present to be consistent with measured experimental values.

Keywords: Iron; Phase transformations; Pressure; Shear; Sequential lamination; Multiscale

*Corresponding author.
E-mail addresses: lewa@stanford.edu (A. Lew), kcasper@princeton.edu (K. Caspersen), eac@princeton.edu (E.A. Carter), ortiz@aero.caltech.edu (M. Ortiz).

0022-5096/$ - see front matter © 2006 Elsevier Ltd. All rights reserved.
doi:10.1016/j.jmps.2005.11.009

1. Introduction

The ground state crystal structure of Fe, ferromagnetic body-centered cubic (bcc), undergoes a stress-induced martensitic phase transformation to a hexagonally close-packed (hcp) structure. Since the pioneering experiments of Bancroft et al. (1956) many attempts have been made to accurately characterize this transformation, with special emphasis in the determination of the transformation pressure (TP), i.e., the value at which the transformation begins (Von Bargen and Boehler, 1990; Rueff et al., 1999; Huang et al., 1987; Barker and Hollenbach, 1974; Taylor et al., 1991b; Giles et al., 1971; Bundy, 1965; Johnson et al., 1962). Although the experimental data is not totally conclusive, several of these studies report that the TP begins at pressures ≈ 9 GPa, and the two phases to coexist up to ≈ 20 GPa. On the other hand, the reverse transition has been seen to start at pressures ranging from 16 GPa to less than 10 GPa, and the two phases to coexist even up to 5 GPa. The observed hysteretic behavior of this phase transition is noteworthy, as well as the degree of uncertainty in the experimental, both dynamic and static, measurements. By comparing the experimental techniques in several of the previous references, Von Bargen and Boehler (1990) hypothesized that softer pressure exerting media used to load the samples lacked control over small amounts of shear deformation, and these were responsible for the associated more prominent hysteretic behavior.

Ab initio methods, mainly Density Functional Theory (DFT), have been used to simulate this transformation (Stixrude et al., 1994; Moroni and Jarlborg, 1996; Cohen et al., 1997; Vočadlo et al., 1997; Söderlind et al., 1995). In most of these studies the relative phase stability was determined by the Gibbs construction, which consists of drawing the line of common tangent between equations of state of pure bcc and hcp. In Ekman et al. (1998), a constrained deformation path between the pure phases was considered; they mapped its energetics via DFT. More generally, martensitic transformations from bcc to hcp have been explored by a variety of theories (Chen et al., 1988; Gornostyrev et al., 1999; Morris and Ho, 2001; Kuznetsov et al., 2001), including short time molecular dynamics simulations of shocked iron samples with lengths of tens to a few hundred nanometers, as shown in Kadau et al. (2002).

Conspicuous among mesoscopic models for martensitic transformations are those based on crystal kinematics and energy minimization, see, e.g., Bhattacharya (2003). The deformation of the atomic lattice is connected to a mesoscopic deformation through the Cauchy–Born hypothesis, and the microstructure morphology is obtained as the one that minimizes the total stored elastic energy under suitable boundary conditions. The application of these models have been strongly biased toward shape memory alloys, with particular emphasis on the study of temperature-induced transformations and small departures from equilibrium for each phase. In contrast, the bcc-to-hcp transformation in iron shows coexistence of the two phases over a rather large range of specific volumes, or more generally, deformations; the nonlinearities in the constitutive behavior of *each phase* need then be included.

An accurate description of the nonlinear energetic landscape for each phase is furnished by ab initio methods, in particular DFT. Occasionally DFT solutions can be invoked on-the-fly in the midst of a microstructural optimization procedure, effectively providing an implicit representation for the energy density (see, e.g., Fago et al., 2004). For more complex materials, such as iron, this may become computationally intractable. One of the

main contribution of this work consists on the design of a viable way to incorporate this type of high-fidelity constitutive descriptions into larger-scale models, Section 2.2. Specifically, we seek to construct and store the energetic landscape a priori, to the desired degree of accuracy, such that the computational cost of evaluation of the nonlinear energy density and its derivatives becomes comparable to that of analytical expressions. It is needless to say that, with the proper validation, such constitutive models may be tailored to be a superior approximation to material behavior over a large range of deformations than phenomenological models fitted to a scattered set of experimental values.

An attractive feature of bcc–hcp phase transitions is that the kinematics of the transformation cannot be described through the deformation of a simple Bravais lattice, given that hcp is not one, but rather of a multi-lattice. The characterization of symmetries of multi-lattices is well-understood for *essential* lattice descriptions (see, e.g., Pitteri and Zanzotto, 2003). However, the transformation herein only admits *nonessential* descriptions, a fact that we overcome by adopting a practical, but perhaps imperfect, solution described in Section 2.1. Moreover, in transformations between two maximal crystal symmetry groups, bcc and hcp, Ericksen–Pitteri neighborhoods, which rationally limit the domain of definition of the elastic energy density, cannot be defined. A strict energy minimization theory predicts that materials for which the domain of definition of the elastic energy density contains an unbounded set of lattice invariant deformations may effectively behave like a fluid (Fonseca, 1987). We sidestep this difficulty by introducing a heuristic argument, hypothesizing that materials are likely to explore more often lattice configurations that are in some sense closer to the reference configuration of the crystal. In practice, this results in limiting the number of consecutive "hops" between phases we perform.

A second chief contribution of this work is the exploration of the role of shear deformations in the TP, motivated by the observations in Von Bargen and Boehler (1990). More generally, we mapped the value of the TP under uniaxial compression of single crystal iron for any direction, an attempt to emulate shock-loading conditions. We found that this type of deformation does not initiate the transformation at low enough pressures to be consistent with experiments, Section 4, hinting the appearance of more complex deformation patterns during experiments.

The content of the paper is as follows. Section 2.1 describes the kinematic description of the transformation, the construction of the elastic energy density is presented in Section 2.2, and the details and results of the extensive DFT computations to map the energetic landscape are included in Section 2.3. We use a sequential lamination algorithm, briefly described in Section 3.1 to obtain the optimal microstructural morphology, and hence the effective macroscopic material behavior. Section 4 shows the aforementioned results on the behavior of iron under different loading patterns. The current paper extends the work in Caspersen et al. (2004) by laying out the model in detail and reporting additional results on the directional dependence of the phase transition.

2. Construction of a first-principles based elastic energy density

We detail next the proposed methodology to construct a first-principle based elastic energy density that accounts for both bcc and hcp phases.

2.1. Kinematics of the transformation

We begin by considering the kinematics of this martensitic transformation. The particular transformation path considered is the one proposed in Mao et al. (1967), depicted in Fig. 1. This mechanism differs from the one proposed in Burgers (1934) by a rotation. Here the hcp lattice is obtained by first applying a shear deformation to a bcc $\{1\,1\,0\}$ plane, consisting of an elongation and compression along perpendicular directions, followed by a shuffle, or shift, of every other deformed $\{1\,1\,0\}$ plane. The need for this shift appears because the bcc structure has a simple Bravais lattice, while the hcp structure needs a multi-lattice. Here and henceforth, all Miller indices are given with respect to the standard cubic and hexagonal bases.

Under these conditions, it is convenient and necessary to choose a multi-lattice representation for the bcc lattice able to describe the above transformation mechanism. One such representation is shown in Fig. 2. In the orthonormal bcc basis, the vectors $\boldsymbol{e}_1 = (1,-1,0)$, $\boldsymbol{e}_2 = (1,1,0)$ and $\boldsymbol{e}_3 = (1/2,-1/2,1/2)$ define a simple Bravais lattice, whereas a second identical lattice has its origin shifted by the vector $\boldsymbol{b} = (1,0,0)$. We denote this type of multi-lattice with $\{\boldsymbol{e}_1,\boldsymbol{e}_2,\boldsymbol{e}_3;\boldsymbol{b}\} \equiv \{\boldsymbol{e}_i;\boldsymbol{b}\}$. All bcc lattice positions can be uniquely represented as a linear combination of the lattice vectors with integer coefficients, plus possibly the shift vector. For an extensive account of the kinematics of multi-lattices we refer the reader to (Pitteri and Zanzotto, 2003).

According to the above mechanism, the hcp lattice is $\{\boldsymbol{U}\boldsymbol{e}_i;\boldsymbol{U}\boldsymbol{b}\pm\boldsymbol{u}\}$, where only one sign is chosen, $\boldsymbol{U}$ is a linear mapping of the lattice vectors, and $\boldsymbol{u}$ is the displacement of every other $\{1\,1\,0\}$ plane in one of the two possible opposite directions. Specifically, for

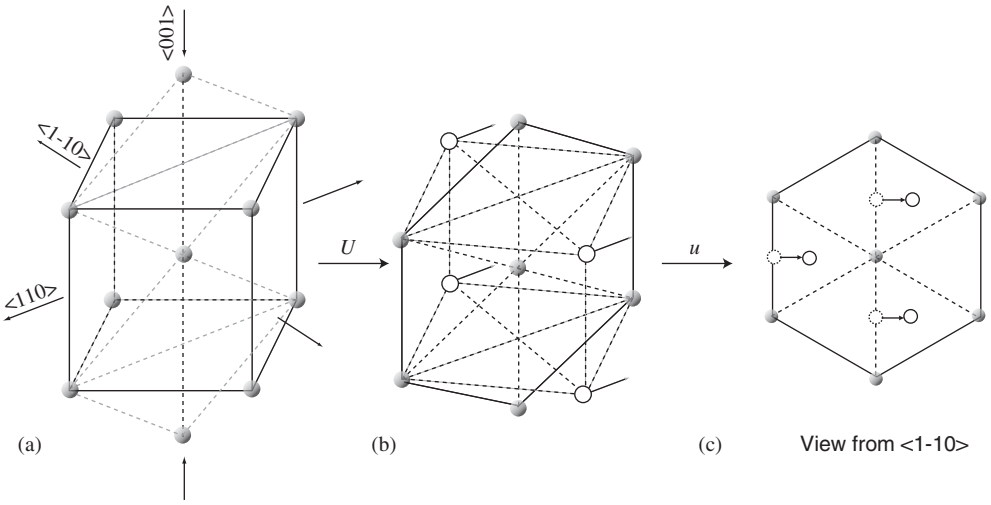

Fig. 1. Proposed mechanism for iron $\alpha \to \varepsilon$ transformation. (a) The lattice deforms through a shear in a $\{1\,1\,0\}$ plane, composed of a stretching and a compression along the $\langle 1\,1\,0\rangle$ and $\langle 0\,0\,1\rangle$ directions, respectively, to form a regular hexagon. The $\langle 1\,\bar{1}\,0\rangle$ direction stretches to accommodate the c/a value of the hcp lattice. This is represented by the affine transformation $\boldsymbol{U}$. (b) The deformed $\{1\,1\,0\}$ plane contains the hcp basal plane. By shifting every other atomic plane parallel to $\{1\,1\,0\}$ by $|\boldsymbol{u}| = a/2\sqrt{3}$, the close-packed structure of hcp is obtained, shown in (c).

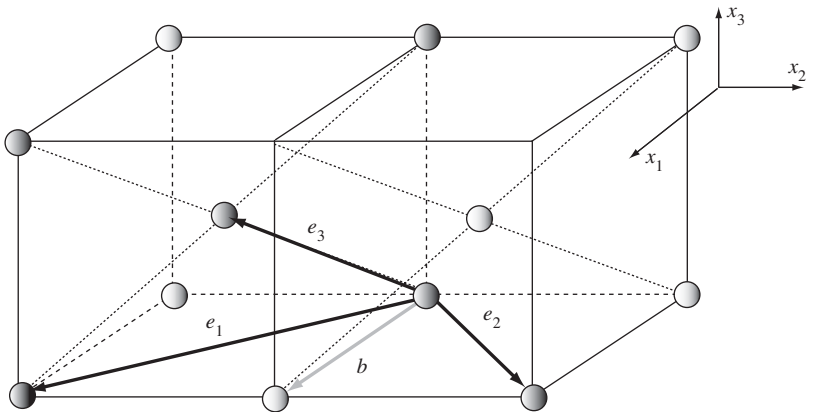

Fig. 2. Multi-lattice representing a bcc atomic arrangement. The atoms of both sub-lattices are represented in black and gray, respectively. The vector $\boldsymbol{b}$ is the shift, or shuffle, between the two sub-lattices. Notice that the resulting atomic lattice possesses bcc symmetry. The use of the two sub-lattices and the shift $\boldsymbol{b}$ permits the representation of the phase transformation mechanism.

(1 1 0) planes

$$\boldsymbol{U}=\begin{pmatrix} \frac{3}{4\sqrt{2}}+\frac{\lambda}{2} & -\frac{3}{4\sqrt{2}}+\frac{\lambda}{2} & 0 \\ -\frac{3}{4\sqrt{2}}+\frac{\lambda}{2} & \frac{3}{4\sqrt{2}}+\frac{\lambda}{2} & 0 \\ 0 & 0 & \frac{\sqrt{3}}{2} \end{pmatrix} \quad \text{and} \quad \boldsymbol{u}=\begin{pmatrix} -\frac{1}{4\sqrt{2}} \\ \frac{1}{4\sqrt{2}} \\ 0 \end{pmatrix}. \tag{1}$$

Here and henceforth all components of vectors and linear transformations are given with respect to the orthonormal bcc basis, unless otherwise stated. In Eq. (1), λ determines the c/a ratio of the deformed cell, i.e., $c/a=\sqrt{\frac{8}{3}}\lambda$, while its volume is given by $\det \boldsymbol{U}=\sqrt{\frac{9}{8}}\lambda$.

Alternative but equivalent mechanisms to obtain undistorted hcp lattices are generated by shearing any of the six {1 1 0} planes in the bcc lattice, and shifting the lattices along the sheared plane back or forth. For transformations of simple Bravais lattices in which no new shift is required, the generation of the linear mappings that describe these mechanisms is straightforward, i.e., these are given by $\boldsymbol{G}^{-1}\boldsymbol{U}\boldsymbol{G}$, with $\boldsymbol{G}$ a symmetry operator in the bcc lattice point group.

For multi-lattices, a proper description requires additional considerations. The most important difference is that for simple Bravais lattices, a symmetry operation $\boldsymbol{G}$ renders new lattice vectors $\{\boldsymbol{G}\boldsymbol{e}_1, \boldsymbol{G}\boldsymbol{e}_2, \boldsymbol{G}\boldsymbol{e}_3\}$ that generate exactly the same set of lattice positions. For the current multi-lattice, however, a symmetry operation of the bcc group acting on it may map lattice vectors in one of the sub-lattices to different sub-lattices. For instance, if $\boldsymbol{G}$ is the π rotation around axis $\boldsymbol{b}$, then the lattice vectors are mapped into $\{\boldsymbol{e}_2, \boldsymbol{e}_1, -\boldsymbol{e}_3+\boldsymbol{b}\}$. This has important consequences when considering the description of the transformation along, for instance, the $(1\,\bar{1}\,0)$ plane. In this case, the lattice is first rotated by π around $\boldsymbol{b}$ to make the $(1\,\bar{1}\,0)$ plane a (1 1 0) plane. The linear mapping and shift from Eq. (1) describe

the bcc → hcp transition in the (1 1 0) plane. However, these were designed to act on the original basis and shift vectors, or multi-lattice description, and not in the rotated ones. It is easy to check that the transformation $\{\boldsymbol{U}\boldsymbol{G}\boldsymbol{e}_i; \boldsymbol{U}\boldsymbol{G}\boldsymbol{b} \pm \boldsymbol{u}\}$ does not give an hcp lattice.

A brief discussion of this pathology in a more general and abstract setting can be found in Pitteri and Zanzotto (2003). Following their treatment, the choice of lattice vectors and shift herein is *nonessential*, i.e., the unit cell of the lattice does not have minimal volume. For *essential* lattice vectors, Proposition 11.2 in (Pitteri and Zanzotto, 2003) guarantees that each individual sub-lattice is mapped into itself after the action of a symmetry operation, up to a rigid body translation. Unfortunately, it is not possible to choose an *essential* set of lattice vectors and shift to describe this transformation, as also pointed out in Pitteri and Zanzotto (2003). Specifically, if a symmetry operation $\boldsymbol{G}$ satisfies

$$\begin{aligned} \boldsymbol{G}\boldsymbol{e}_i &= n_i^k \boldsymbol{e}_k, \\ \boldsymbol{G}\boldsymbol{b} &= \ell^k \boldsymbol{e}_k + \delta \boldsymbol{b}, \end{aligned} \tag{2}$$

then each individual lattice is mapped into itself, modulo a rigid body translation. Here n_i^k and ℓ^k are integers, $|\delta| = 1$ and the repeated indices summation convention has been adopted. For a multi-lattice with an essential set of lattice vectors and shift, these conditions are necessary and sufficient for $\boldsymbol{G}$ to be a symmetry operation, as shown in Pitteri and Zanzotto (2003) and also discussed in (Pitteri, 1985; Ericksen, 1999, 1970). From the above example, we see that the symmetry group of the multi-lattice contains members that do not satisfy Eq. (2) in our case.

This loss of symmetry of each individual lattice is intimately related to the arbitrary choice of a multi-lattice representation among the multiple equivalent ones. A natural and simple solution therefore is choosing a possibly different set of lattice vectors and shift for each group operation $\boldsymbol{G}$. A similar idea is also mentioned in (Pitteri and Zanzotto, 2003; Ericksen, 1997). One convenient choice is $\{\boldsymbol{e}_i^{\boldsymbol{G}}; \boldsymbol{b}^{\boldsymbol{G}}\}$, where $\boldsymbol{e}_i^{\boldsymbol{G}} = \boldsymbol{G}^{-1}\boldsymbol{e}_i$ and $\boldsymbol{b}^{\boldsymbol{G}} = \boldsymbol{G}^{-1}\boldsymbol{b}$. The alternative hcp lattices, or variants, are then given by $\{\boldsymbol{G}^{-1}\boldsymbol{U}\boldsymbol{G}\boldsymbol{e}_i^{\boldsymbol{G}}; \boldsymbol{G}^{-1}(\boldsymbol{U}\boldsymbol{G}\boldsymbol{b}^{\boldsymbol{G}} \pm \boldsymbol{u})\}$, for each $\boldsymbol{G}$ in the bcc point group. A simple interpretation for this formulae is that $\boldsymbol{G}$ first rotates the {1 1 0} plane that contains $\boldsymbol{e}_1^{\boldsymbol{G}}$ and $\boldsymbol{e}_2^{\boldsymbol{G}}$ to coincide with the plane (1 1 0), where the transformation of the lattice according to Eq. (1) can be used. The inverse mapping $\boldsymbol{G}^{-1}$ then rotates the new hcp lattice back and gives a symmetric matrix, but any other rigid rotation could have been used as well. As expected, many of the elements of the bcc point group and choices of shift directions generate the same mechanisms. For example, $(\boldsymbol{G}^{-1}\boldsymbol{U}\boldsymbol{G}\boldsymbol{e}_i^{\boldsymbol{G}}; \boldsymbol{G}^{-1}(\boldsymbol{U}\boldsymbol{G}\boldsymbol{b}^{\boldsymbol{G}} + \boldsymbol{u})$ is also generated by $\tilde{\boldsymbol{G}}$ and the choice of the minus sign for $\boldsymbol{u}$, where $\tilde{\boldsymbol{G}}$ results from the composition of $\boldsymbol{G}$ and a reflection with respect to the plane orthogonal to $\boldsymbol{e}_1^{\boldsymbol{G}}$. A total of 12 different mechanisms are thus obtained, but only 6 different symmetric linear mappings or hcp variants $\boldsymbol{G}^{-1}\boldsymbol{U}\boldsymbol{G}$. For completeness, these are listed in Table 1. Each variant $\boldsymbol{U}^\alpha$, $\alpha = 1, \ldots, 6$, therein is generated by some group operation $\boldsymbol{G}^\alpha$ readily identified from $\boldsymbol{U}^\alpha$ by the {1 1 0} plane in which the hcp basal plane forms. The multi-lattice description is completed with the corresponding shift $\boldsymbol{u}^\alpha$ shown in Table 2 as $\{\boldsymbol{U}^\alpha \boldsymbol{e}_i^\alpha; \boldsymbol{U}^\alpha(\boldsymbol{b}^\alpha \pm \boldsymbol{u}^\alpha)\}$, where $\boldsymbol{e}_i^\alpha$ and $\boldsymbol{b}^\alpha$ are the original bcc set of lattice vectors and shift chosen to describe the deformation with $\boldsymbol{G}^\alpha$. The ± sign in front of $\mathbf{u}^\alpha$ reflects the fact that $\mathbf{G}$ and $-\mathbf{G}$ generate the same $\mathbf{U}^\alpha$, but opposite $\mathbf{u}^\alpha$.

Each hcp variant can transform back to a bcc lattice by simply reversing the shift and the shear deformation along hcp basal planes. As shown in Fig. 3, for a given variant there are three symmetry-related equivalent ways of shifting back every {0 0 0 2} plane before

Table 1
Symmetric transformations generating the hcp variants $\boldsymbol{G}^{-1}\boldsymbol{U}\boldsymbol{G}$, given in the bcc orthogonal basis

$$\boldsymbol{U}^1=\begin{pmatrix}\frac{3}{4\sqrt{2}}+\frac{\lambda}{2} & -\frac{3}{4\sqrt{2}}+\frac{\lambda}{2} & 0\\ -\frac{3}{4\sqrt{2}}+\frac{\lambda}{2} & \frac{3}{4\sqrt{2}}+\frac{\lambda}{2} & 0\\ 0 & 0 & \frac{\sqrt{3}}{2}\end{pmatrix}\quad \boldsymbol{U}^2=\begin{pmatrix}\frac{3}{4\sqrt{2}}+\frac{\lambda}{2} & \frac{3}{4\sqrt{2}}-\frac{\lambda}{2} & 0\\ \frac{3}{4\sqrt{2}}-\frac{\lambda}{2} & \frac{3}{4\sqrt{2}}+\frac{\lambda}{2} & 0\\ 0 & 0 & \frac{\sqrt{3}}{2}\end{pmatrix}$$

$$\boldsymbol{U}^3=\begin{pmatrix}\frac{3}{4\sqrt{2}}+\frac{\lambda}{2} & 0 & \frac{3}{4\sqrt{2}}-\frac{\lambda}{2}\\ 0 & \frac{\sqrt{3}}{2} & 0\\ \frac{3}{4\sqrt{2}}-\frac{\lambda}{2} & 0 & \frac{3}{4\sqrt{2}}+\frac{\lambda}{2}\end{pmatrix}\quad \boldsymbol{U}^4=\begin{pmatrix}\frac{3}{4\sqrt{2}}+\frac{\lambda}{2} & 0 & -\frac{3}{4\sqrt{2}}+\frac{\lambda}{2}\\ 0 & \frac{\sqrt{3}}{2} & 0\\ -\frac{3}{4\sqrt{2}}+\frac{\lambda}{2} & 0 & \frac{3}{4\sqrt{2}}+\frac{\lambda}{2}\end{pmatrix}$$

$$\boldsymbol{U}^5=\begin{pmatrix}\frac{\sqrt{3}}{2} & 0 & 0\\ 0 & \frac{3}{4\sqrt{2}}+\frac{\lambda}{2} & -\frac{3}{4\sqrt{2}}+\frac{\lambda}{2}\\ 0 & -\frac{3}{4\sqrt{2}}+\frac{\lambda}{2} & \frac{3}{4\sqrt{2}}+\frac{\lambda}{2}\end{pmatrix}\quad \boldsymbol{U}^6=\begin{pmatrix}\frac{\sqrt{3}}{2} & 0 & 0\\ 0 & \frac{3}{4\sqrt{2}}+\frac{\lambda}{2} & \frac{3}{4\sqrt{2}}-\frac{\lambda}{2}\\ 0 & \frac{3}{4\sqrt{2}}-\frac{\lambda}{2} & \frac{3}{4\sqrt{2}}+\frac{\lambda}{2}\end{pmatrix}$$

The multi-lattice description used to generate each variant is readily obtained by identifying the {1 1 0} plane where the hcp basal plane forms.

Table 2
Shift vectors $\boldsymbol{G}^{-1}\boldsymbol{U}\boldsymbol{u}$ corresponding to each one of the hcp variants in Table 1

$$\boldsymbol{u}^1=\begin{pmatrix}-\frac{1}{4}\\ \frac{1}{4}\\ 0\end{pmatrix}\quad \boldsymbol{u}^2=\begin{pmatrix}\frac{1}{6}\\ \frac{1}{6}\\ 0\end{pmatrix}\quad \boldsymbol{u}^3=\begin{pmatrix}\frac{1}{6}\\ 0\\ \frac{1}{6}\end{pmatrix}\quad \boldsymbol{u}^4=\begin{pmatrix}-\frac{1}{6}\\ 0\\ \frac{1}{6}\end{pmatrix}\quad \boldsymbol{u}^5=\begin{pmatrix}0\\ -\frac{1}{6}\\ \frac{1}{6}\end{pmatrix}\quad \boldsymbol{u}^6=\begin{pmatrix}0\\ \frac{1}{6}\\ \frac{1}{6}\end{pmatrix}$$

Each hcp variant is given by the multi-lattice $\{\boldsymbol{U}^\alpha\boldsymbol{e}_i^\alpha;\boldsymbol{U}^\alpha(\boldsymbol{b}^\alpha\pm\boldsymbol{u}^\alpha)\}$, with $\alpha=1,\ldots,6$. The multi-lattice description $(\boldsymbol{e}_i^\alpha;\boldsymbol{b}^\alpha)$ used to generate each variant is readily obtained by identifying the {1 1 0} plane in which the hcp basal plane forms; the plane orthogonal to the eigenvector with unit eigenvalue in $\boldsymbol{U}^\alpha$.

deforming the plane, and only one of these is the exact inverse of the forward transformation. In this case, the application of the inverse shear deformation returns the original bcc lattice, whereas the other two cases return bcc lattices where, for instance, cube diagonals become cube edges; see Fig. 3. Since six hcp variants have been identified thus far, all reverse transformations produce 12 additional bcc variants.

We next obtain the expressions for the lattices of these variants. To this end, let $\boldsymbol{H}$ denote a symmetry operation in the hcp point group of a variant generated by $\boldsymbol{U}$. Fortunately, all hcp symmetry operations and the basis at each variant satisfy the conditions in Eq. (2), as can be easily checked. A simple way to do this is to note that no symmetry operation in the hcp point group maps a {0 0 0 1} plane into a {0 0 0 2} plane, and as a consequence the two lattices are mapped into themselves. The action of $\boldsymbol{H}$ on $\{\boldsymbol{U}\boldsymbol{e}_i;\boldsymbol{U}\boldsymbol{b}+\boldsymbol{u}\}$ thus returns the lattice $\{\boldsymbol{H}\boldsymbol{U}\boldsymbol{e}_i;\boldsymbol{H}(\boldsymbol{U}\boldsymbol{b}+\boldsymbol{u})\}$. More generally, the same

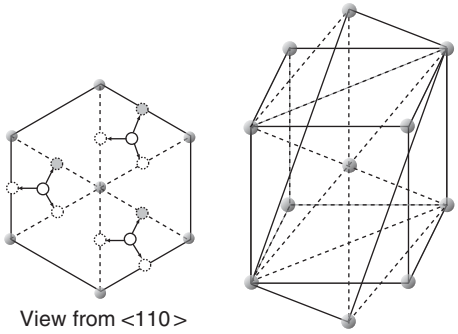

Fig. 3. The three equivalent displacements of every other {0 0 0 2} plane are shown on the left. To illustrate the difference between these choices, the figure on the right shows in gray the rectangle in the original bcc lattice that, through one of the inverse deformations from hcp, becomes the diagonal plane joining two parallel edges in the new cube. This corresponds to choosing the shifted atoms in gray in the figure on the left.

Table 3
Linear transformations $\boldsymbol{G}^{-1}\boldsymbol{U}^{-1}\boldsymbol{H}\boldsymbol{U}\boldsymbol{G}$ generating the 12 bcc variants considered here expressed in the bcc orthogonal basis

$$\boldsymbol{U}^{7}=\tfrac{1}{4}\begin{pmatrix}1&3&2\\3&1&-2\\-3&3&-2\end{pmatrix}\quad \boldsymbol{U}^{8}=\tfrac{1}{4}\begin{pmatrix}1&3&-2\\3&1&2\\3&-3&-2\end{pmatrix}\quad \boldsymbol{U}^{9}=\tfrac{1}{4}\begin{pmatrix}1&-3&2\\-3&1&2\\-3&-3&-2\end{pmatrix}$$

$$\boldsymbol{U}^{10}=\tfrac{1}{4}\begin{pmatrix}1&-3&-2\\-3&1&-2\\3&3&-2\end{pmatrix}\quad \boldsymbol{U}^{11}=\tfrac{1}{4}\begin{pmatrix}1&-2&-3\\3&-2&3\\-3&-2&1\end{pmatrix}\quad \boldsymbol{U}^{12}=\tfrac{1}{4}\begin{pmatrix}1&2&-3\\-3&-2&-3\\-3&2&1\end{pmatrix}$$

$$\boldsymbol{U}^{13}=\tfrac{1}{4}\begin{pmatrix}1&-2&3\\3&-2&-3\\3&2&1\end{pmatrix}\quad \boldsymbol{U}^{14}=\tfrac{1}{4}\begin{pmatrix}1&2&3\\-3&-2&3\\3&-2&1\end{pmatrix}\quad \boldsymbol{U}^{15}=\tfrac{1}{4}\begin{pmatrix}-2&-3&3\\2&1&3\\-2&3&1\end{pmatrix}$$

$$\boldsymbol{U}^{16}=\tfrac{1}{4}\begin{pmatrix}-2&3&-3\\-2&1&3\\2&3&1\end{pmatrix}\quad \boldsymbol{U}^{17}=\tfrac{1}{4}\begin{pmatrix}-2&-3&-3\\2&1&-3\\2&-3&1\end{pmatrix}\quad \boldsymbol{U}^{18}=\tfrac{1}{4}\begin{pmatrix}-2&3&3\\-2&1&-3\\-2&-3&1\end{pmatrix}$$

The 13th variant $\boldsymbol{U}^{0}$ is, of course, the identity. The {1 1 0} plane along which the shearing takes place is orthogonal to the only eigenvector with unit eigenvalue for each matrix. This eigenvector simultaneously defines the multi-lattice representation used to generate the matrix. For notational simplicity, we give matrices with rational coefficients, instead of their symmetric parts. Also, when transformed into their respective multi-lattice bases, these matrices acquire integer coefficients so that exactly the same original bcc lattice positions are recovered.

symmetry operation $\boldsymbol{H}$ on a different hcp variant $\boldsymbol{G}^{-1}\boldsymbol{U}\boldsymbol{G}$ is $\boldsymbol{G}^{-1}\boldsymbol{H}\boldsymbol{G}$, and gives the lattice positions $\{\boldsymbol{G}^{-1}\boldsymbol{H}\boldsymbol{U}\boldsymbol{G}\boldsymbol{e}_i^{\boldsymbol{G}};\boldsymbol{G}^{-1}\boldsymbol{H}(\boldsymbol{U}\boldsymbol{G}\boldsymbol{b}^{\boldsymbol{G}}+\boldsymbol{u})\}$. The reverse transformation ensues by changing the shift by $-\boldsymbol{G}^{-1}\boldsymbol{u}$ and transforming the lattice vectors with $\boldsymbol{G}^{-1}\boldsymbol{U}^{-1}\boldsymbol{G}$. Hence, the lattices of all bcc variants identified thus far are $\{\boldsymbol{G}^{-1}\boldsymbol{U}^{-1}\boldsymbol{H}\boldsymbol{U}\boldsymbol{G}\boldsymbol{e}_i^{\boldsymbol{G}};\boldsymbol{G}^{-1}\boldsymbol{U}^{-1}(\boldsymbol{H}\boldsymbol{U}\boldsymbol{G}\boldsymbol{b}^{\boldsymbol{G}}+(\boldsymbol{H}-\boldsymbol{I})\boldsymbol{u})\}$, where $\boldsymbol{I}$ is the identity. The list of the linear transformations for these additional 12 bcc variants are shown in Table 3. For completeness, Table 4 provides the values of the shift vectors $\boldsymbol{G}^{-1}\boldsymbol{U}^{-1}\boldsymbol{H}^{-1}(\boldsymbol{H}-\boldsymbol{I})\boldsymbol{u}$ as well.

Additional bcc and hcp lattices could be obtained via further transformations from the newly obtained variants, however we confine ourselves to the 19 variants identified thus

Table 4
Shift vectors $\boldsymbol{G}^{-1}\boldsymbol{U}^{-1}\boldsymbol{H}^{-1}(\boldsymbol{H}-\boldsymbol{I})\boldsymbol{u}$ corresponding to each one of the bcc variants in Table 3

$\boldsymbol{u}^7=\frac{1}{4}\begin{pmatrix}-1\\1\\1\end{pmatrix}$	$\boldsymbol{u}^8=\frac{1}{4}\begin{pmatrix}-1\\1\\-1\end{pmatrix}$	$\boldsymbol{u}^9=\frac{1}{4}\begin{pmatrix}1\\1\\-1\end{pmatrix}$	$\boldsymbol{u}^{10}=\frac{1}{4}\begin{pmatrix}1\\1\\1\end{pmatrix}$
$\boldsymbol{u}^{11}=\frac{1}{4}\begin{pmatrix}1\\1\\1\end{pmatrix}$	$\boldsymbol{u}^{12}=\frac{1}{4}\begin{pmatrix}1\\-1\\1\end{pmatrix}$	$\boldsymbol{u}^{13}=\frac{1}{4}\begin{pmatrix}-1\\-1\\1\end{pmatrix}$	$\boldsymbol{u}^{14}=\frac{1}{4}\begin{pmatrix}-1\\1\\1\end{pmatrix}$
$\boldsymbol{u}^{15}=\frac{1}{4}\begin{pmatrix}1\\-1\\1\end{pmatrix}$	$\boldsymbol{u}^{16}=\frac{1}{4}\begin{pmatrix}-1\\-1\\1\end{pmatrix}$	$\boldsymbol{u}^{17}=\frac{1}{4}\begin{pmatrix}-1\\1\\1\end{pmatrix}$	$\boldsymbol{u}^{18}=\frac{1}{4}\begin{pmatrix}1\\1\\1\end{pmatrix}$

Each bcc variant is given by the multi-lattice $\{\boldsymbol{U}^\alpha\boldsymbol{e}_i^\alpha;\boldsymbol{U}^\alpha(\boldsymbol{b}^\alpha\pm\boldsymbol{u}^\alpha)\}$, with $\alpha=7,\ldots,18$. The multi-lattice description $(\boldsymbol{e}_i^\alpha;\boldsymbol{b}^\alpha)$ used to generate each variant is readily obtained by identifying the $\{1\,1\,0\}$ plane in which the hcp basal plane forms; the plane orthogonal to the eigenvector with unit eigenvalue in $\boldsymbol{U}^\alpha$.

far. The continuation of this process may eventually lead to an infinite number of different variants. The situation is akin, but not identical, to the one described in Bhattacharya et al. (2004). Therein, conditions for the existence of an infinite number of variants were explicitly stated, and simple examples were constructed by the recursive application of simple shear deformations in a two-dimensional setting. We note that in our case unbounded atomic displacements can only be obtained by alternative application of bcc to bcc deformation mechanisms acting on different $\{1\,1\,0\}$ planes. It is simple to check that variants $\{\boldsymbol{U}^{2i-1},\boldsymbol{U}^{2i}\}$, $i=4,\ldots,9$, act on the same plane, have the same multi-lattice basis and form a finite symmetry group for each one of the sub-lattices. Describing the consecutive application of deformation mechanisms on different $\{1\,1\,0\}$ planes may require an expanded kinematic description, to account for the change of multi-lattice representation needed at the intermediate stage.

The foregoing analysis has been concerned with the identification of variants. We subsequently analyze how affine deformations act on each one of these variants yielding a new atomic arrangement. As alluded before, an affine deformation $\boldsymbol{F}$ deforms a multi-lattice $\{\boldsymbol{e}_i,\boldsymbol{b}\}$ by transforming it into $\{\boldsymbol{F}\boldsymbol{e}_i,\boldsymbol{F}\boldsymbol{b}\}$. Then, a variant α, $\alpha=0,\ldots,18$, is obtained by the action of the affine deformation $\boldsymbol{U}^\alpha$ on the multi-lattice $\{\boldsymbol{e}_i^\alpha;\boldsymbol{b}^\alpha\pm\boldsymbol{u}^\alpha\}$, i.e., $\{\boldsymbol{U}^\alpha\boldsymbol{e}_i^\alpha;\boldsymbol{U}^\alpha(\boldsymbol{b}^\alpha\pm\boldsymbol{u}^\alpha)\}$. Here $\boldsymbol{U}^\alpha$ is any of the affine deformations given in Tables 1 and 3, while $\boldsymbol{u}^\alpha$ are the associated shifts given in Tables 2 and 4. It is then useful to interpret $\{\boldsymbol{e}_i^\alpha;\boldsymbol{b}^\alpha\pm\boldsymbol{u}^\alpha\}$ as a reference lattice for variant α, in which the shifting of atomic planes from the original bcc atomic arrangement occurs a priori, while the affine deformation leading to the variant occurs a posteriori. More generally, an affine deformation $\boldsymbol{F}$ deforms variant α to give the atomic lattice $\{\boldsymbol{F}\boldsymbol{e}_i^\alpha;\boldsymbol{F}(\boldsymbol{b}^\alpha\pm\boldsymbol{u}^\alpha)\}$.This last expression is in stark contrast with descriptions in which no shifting of atomic planes is needed. In the latter, there is only one reference atomic arrangement that is deformed affinely, while herein we have a different reference lattice for each variant.

2.2. Energetics

We confine our attention to transformations occurring at 0 K and therefore the governing principle is energy minimization. In particular, the formation of microstructure

is driven purely by energetics. We assume the behavior of the material to be nonlinear elastic with energy density $W(\boldsymbol{F})$, where $\boldsymbol{F}$ is the local deformation gradient (Marsden and Hughes, 1994). The function $W(\boldsymbol{F})$ must be invariant under rigid-body rotations, and, therefore it must be of the form $W(\boldsymbol{C})$, where $\boldsymbol{C} = \boldsymbol{F}^{\mathsf{T}}\boldsymbol{F}$ is the right Cauchy–Green deformation tensor (Marsden and Hughes, 1994). In addition, if $\mathscr{G} \subset SO(3)$ is the point symmetry group of the crystal in its reference configuration, then we must have $W(\boldsymbol{FG}) = W(\boldsymbol{F})$ for all $\boldsymbol{G}$ in $\mathscr{G}$.

We connect the macroscopic deformation gradient $\boldsymbol{F}$ and the atomic arrangement of variant α via the Cauchy–Born hypothesis (Ericksen, 1984), which assumes that the lattice of variant α is locally uniformly deformed according to the macroscopic deformation gradient. This hypothesis has been widely used in the mathematical analysis of martensites (Bhattacharya, 2003). We are interested in building functions $W^{\alpha}(\boldsymbol{F})$, $\alpha = 0, \ldots, 18$, such that $W^{\alpha}(\boldsymbol{F})$ returns the energy per unit mass of the atomic arrangement that follows after deforming variant α with an affine deformation $\boldsymbol{F}$. The material's energy per unit mass $W(\boldsymbol{F})$ ensues by finding that atomic arrangement that gives the lowest energy among all variants with the given affine deformation, i.e.,

$$W(\boldsymbol{F}) = \min_{\alpha=0,\ldots,18} W^{\alpha}(\boldsymbol{F}). \tag{3}$$

Each function $W^{\alpha}(\mathbf{F})$ must also be invariant under superimposed rigid body rotations, so that $W(\mathbf{F})$ is. Therefore $W^{\alpha}(\mathbf{F})$ can only depend on $\boldsymbol{C} = \boldsymbol{F}^{\mathsf{T}}\boldsymbol{F}$, i.e., $W^{\alpha}(\boldsymbol{F}) = A^{\alpha}(\boldsymbol{C})$, and consequently $W(\boldsymbol{F}) = A(\boldsymbol{C})$.

The energy density A^{α} for any given periodic atomic arrangement can be calculated from quantum mechanics, by using for instance, DFT. Nevertheless, computations of this type are often computationally expensive, preventing them from being performed *on-the-fly* as part of a calculation at a larger scale, such as a finite element simulation or a microstructural optimization. In these situations, we need to a priori generate an interpolation of each function A^{α} as a function of $\boldsymbol{C}$. The unquestionable advantage of this approach is that we need only to compute the function A^{α} *once*, to any desired degree of accuracy. The uncertainties of the nonlinear elastic model stem hereafter from the use of DFT, in contrast to more traditional phenomenological descriptions that rely heavily on the judicious choice of the functional form for the strain energy density.

An accurate interpolation of a smooth function in six dimensions may be possible, but not practical. Instead, we adopt the perspective that elastic shear deformations cannot be very large before plastic deformation is obtained. We would like to construct highly accurate approximations of the energy density and its derivatives for a large range of volumetric changes, but with relatively small shears. One possibility, adopted here, consists of performing a Taylor series expansion of the energy density around local equilibria, as defined below.

Briefly, the energy density for each phase is constructed as follows. At each volume V, we compute exactly from first principles the energy of the lowest-energy configuration of that phase at the given volume. For any other configuration at volume V of the same phase, we approximate its energy through a second-order Taylor expansion centered at the lowest-energy configuration at volume V. We provide a thorough description of this idea next.

We assume that the lattice $\{\boldsymbol{e}_i^0, \boldsymbol{b}^0\}$ describes the unstressed bcc lattice, and therefore, it is in equilibrium. We slowly change the unit cell volume of the bcc phase, equilibrating the

resulting lattice at each volume step. We obtain in this way a function $\boldsymbol{C}^0(V)$, such that $\boldsymbol{C}^0(V_0) = (\boldsymbol{U}^0)^{\mathsf{T}}\boldsymbol{U}^0$ with V_0 the volume of $\{\boldsymbol{e}_i^0, \boldsymbol{b}^0\}$. The function $\boldsymbol{C}^0(V)$ satisfies that it is a local energy minimizer among all neighboring affine deformations of $\{\boldsymbol{e}_i^0, \boldsymbol{b}^0\}$ at volume V. The continuation procedure makes the resulting function continuous, and the problem well-defined. We have not found bifurcations in the range of volumes explored. The symmetry of bcc lattices, and the fact that we did not find bifurcations, made the function $\boldsymbol{C}^0(V)$ be very simple, in fact $\boldsymbol{C}^0(V) = (V/V^0)^{2/3}\boldsymbol{I}$. The analogous functions $\boldsymbol{C}^\alpha(V)$, $\alpha = 7, \ldots, 18$, for the remaining bcc variants then follow naturally as $\boldsymbol{C}^\alpha(V) = (V/V^0)^{2/3}(\boldsymbol{U}^\alpha)^{\mathsf{T}}\boldsymbol{U}^\alpha$.

The situation is more interesting in the hcp case. Here, by varying the values of the hcp lattice parameters a and c we can have a variety of lattices at the same volume without breaking the hcp symmetry. We proceed first by finding the value of λ that equilibrates $\boldsymbol{U}^\alpha$, $\alpha = 1, \ldots, 6$. The continuation procedure is then performed, which serves to determine the value of c/a at each specific volume, shown in Fig. 4, or the function $\lambda(V) = \sqrt{\frac{3}{8}}(c/a)(V)$. No bifurcations have been observed here either, for the range of unit cell volumes explored. Consequently, if $\boldsymbol{E}_i^\alpha = \boldsymbol{U}^\alpha \boldsymbol{e}_i^\alpha / (\det \boldsymbol{U}^\alpha)^{1/3}$ and $\boldsymbol{E}^{\alpha,i}$ is a vector in the reciprocal basis, then $\boldsymbol{C}^\alpha(V) = (\boldsymbol{K}^\alpha)^{\mathsf{T}}(V)\boldsymbol{K}^\alpha(V)$, where

$$\boldsymbol{K}^\alpha(V) = \left(\frac{V\lambda(V_0)}{V_0\lambda(V)}\right)^{1/3}\left[\boldsymbol{E}_1^\alpha \otimes \boldsymbol{E}^{\alpha,1} + \boldsymbol{E}_2^\alpha \otimes \boldsymbol{E}^{\alpha,2} + \frac{\lambda(V)}{\lambda(V_0)}\boldsymbol{E}_3^\alpha \otimes \boldsymbol{E}^{\alpha,3}\right].$$

The defining characteristic of lattices given by $\boldsymbol{C}^\alpha(V)$ is that they are local energy minimizers among all nearby lattices with the same volume.

The approximate energy density $\hat{W}$, valid for small shears away from the equilibrium lattice at each lattice volume, is proposed to be

$$\hat{W}^\alpha(\boldsymbol{C}) = \hat{W}_0^\alpha(V) + \tfrac{1}{2}[\boldsymbol{C} - \boldsymbol{C}^\alpha(V)] : \mathbb{C}^\alpha(V) : [\boldsymbol{C} - \boldsymbol{C}^\alpha(V)], \tag{4}$$

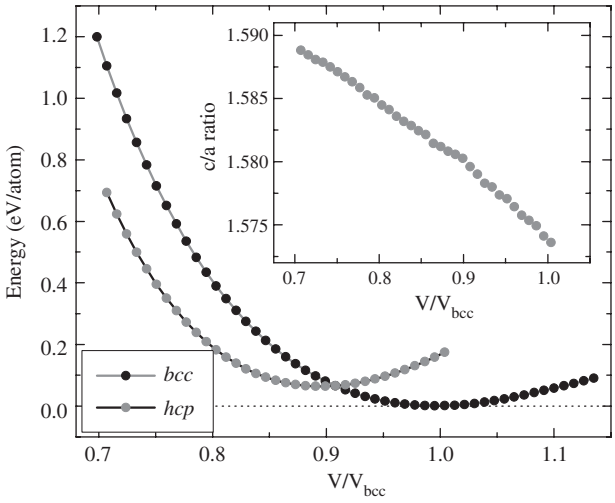

Fig. 4. The equations of state for the bcc and hcp phases. The inset shows the optimal c/a ratio of the hcp phase as a function of volume.

where $V = V_0\sqrt{\det \boldsymbol{C}}$ is the volume of the deformed lattice, and $\hat{W}_0^\alpha(V) = W^\alpha(\boldsymbol{C}^\alpha(V))$ and $\mathbb{C}^\alpha(V) = \partial^2 W^\alpha/\partial \boldsymbol{C}^2(\boldsymbol{C}^\alpha(V))$ are the energy density and the material elastic moduli at the equilibrium lattice as a function of lattice volume, respectively. The first-order term in the Taylor expansion is identically zero by definition of $\boldsymbol{C}^\alpha(V)$. The values of $\hat{W}_0^\alpha(V)$ and $\mathbb{C}^\alpha(V)$ are all obtained directly from the first-principles computations.

2.3. Density Functional Theory computations

The first-principles method we use to calculate $\boldsymbol{C}^\alpha(V)$, $\hat{W}_0^\alpha(V)$, and $\mathbb{C}^\alpha(V)$ is Kohn–Sham DFT (Kohn and Sham, 1965). In order to accurately recover the magnetic and structural properties of Fe, the Projector Augmented Wave (PAW) all-electron method (Blöchl, 1994) is used. The correct phase ordering is achieved by employing the PW-91 Generalized Gradient Approximation (GGA) exchange-correlation functional (Perdew et al., 1992). Highly precise DFT calculations are required for the determination of the elastic moduli (Steinle-Neumann et al., 1999); to this end, we use a 500 eV kinetic energy cutoff for the planewave basis (which converges the total energy of the unit cell to within 1 meV/atom) and a $(24 \times 24 \times 24)$ Monkhorst–Pack (Monkhorst and Pack, 1976) k-point grid for the two-atom unit cell. Since the bcc phase is magnetic, spin-polarized calculations are used for this phase. All calculations are performed using the Vienna Ab Initio Simulations Package (VASP) (Kresse and Furthmüller, 1996).

The calculated equations of state for the two phases and the c/a ratio of the hcp phase are shown in Fig. 4. A comparison of our PAW calculations to experimentally measured values (Knittle, 1995) and Linear Augmented Plane Wave (LAPW) calculations (Stixrude et al., 1994) are shown in Table 5. The PAW calculations on the bcc phase are in reasonable agreement with experiment and the LAPW calculations for the equilibrium bulk modulus ($B^{\text{bcc}}(V_{\text{bcc}})$) and magnetic moment ($\mu_0$); however, both PAW and LAPW predict the equilibrium volume of the bcc phase (V_{bcc}) to be slightly smaller than experimental measurements. The PAW calculations on the hcp phase compare well with the LAPW calculations; however, both methods deviate significantly from experiment. This deviation could be caused by an inexact extrapolation of the experimental values to zero temperature and pressure. Alternatively, there is speculation that the hcp phase may be anti-ferromagnetic rather than non-magnetic at low pressures (Steinle-Neumann et al., 1999). This could explain the discrepancy between experiment and theory,

Table 5
A comparison of the our PAW calculations with experimental measurements and LAPW calculations

	bcc			hcp			TP
	V_{bcc}	$B^{\text{bcc}}(V_{\text{bcc}})$	μ_0	V_{hcp}	$B^{\text{hcp}}(V_{\text{hcp}})$	c/a	
Experiment[a]	11.69	162–176	2.22[b]	11.2	208	1.61	10–15
LAPW[c]	11.40	189	2.17	10.20	291	1.58	11
PAW[d]	11.46	188	2.21	10.26	288	1.58	10

The units for volume, pressure, and magnetic moment are Å^3, GPa, and Bohr magneton, respectively.
[a]Knittle (1995).
[b]Ashcroft and Mermin (1976).
[c]Stixrude et al. (1994).
[d]This work.

since the calculations were performed assuming the hcp phase is non-magnetic for all pressures. It is also possible to approximate the transformation pressure (TP) using the above-mentioned Gibbs construction, where the approximate TP is given by the slope of the line of common tangent between the two phases. As shown in Table 5, our PAW calculations compare well with the LAPW calculations and fall within the experimentally measured range.

The elastic constants are calculated by utilizing the relationship they have with the bulk modulus, the volume dependence of c/a ratio for the hcp phase, and specific volume conserving shears (performed similarly to the work of Cohen et al., 1997). The bulk modulus for both the bcc ($B^{\text{bcc}}(V)$) and hcp ($B^{\text{hcp}}(V)$) phases can be defined in terms of elastic constants as

$$B^{\text{bcc}}(V) = \tfrac{1}{3}(C_{11}(V) + 2C_{12}(V)), \tag{5}$$

$$B^{\text{hcp}}(V) = \frac{C_{33}(V)[C_{11}(V) + C_{12}(V)] - 2C_{13}^2(V)}{C_{11}(V) + C_{12}(V) + 2C_{33}(V) - 4C_{13}(V)}, \tag{6}$$

where we adopted Voigt notation for the moduli. To determine the bulk modulus as a function of volume, the fitted Murnaghan's equations of state for both phases are differentiated with respect to volume. The volume dependence of the c/a ratio for the hcp phase is related to the elastic constants through the dimensionless quantity $R(V)$, where

$$R(V) = -\frac{\partial \ln(c/a)}{\partial \ln(V/V_{\text{bcc}})} = \frac{C_{33}(V) - C_{11}(V) - C_{12}(V) + C_{13}(V)}{C_{11}(V) + C_{12}(V) + 2C_{33}(V) - 4C_{13}(V)}. \tag{7}$$

We determine $R(V)$ by differentiating a third order polynomial that is fit to $\ln(c/a)$ vs. $\ln(V/V_{\text{bcc}})$.

Eq. (5) gives one relation of the bcc elastic constants to a calculated quantity. Similarly, Eqs. (6) and (7)) give two relations of the hcp elastic constants to calculated quantities. The remaining relations needed to fully determine the elastic constants are obtained by computing the energy changes upon perturbing the crystal with small volume-conserving shears. If $\boldsymbol{F}^0$ represents the unperturbed lattice, then $\boldsymbol{F}^{\varepsilon} = (\boldsymbol{I} + \boldsymbol{\varepsilon})\boldsymbol{F}^0$ represents the lattice after the application of a shear deformation $\boldsymbol{\varepsilon}$. By symmetry, it is enough for the bcc phase to apply two different types of shear, $\varepsilon_t^{\text{bcc}}$ and $\varepsilon_s^{\text{bcc}}$, given by

$$\boldsymbol{\varepsilon}_t^{\text{bcc}} = \begin{pmatrix} \varepsilon & 0 & 0 \\ 0 & -\varepsilon & 0 \\ 0 & 0 & \dfrac{\varepsilon^2}{1-\varepsilon^2} \end{pmatrix} \quad \text{and} \quad \boldsymbol{\varepsilon}_s^{\text{bcc}} = \begin{pmatrix} 0 & \varepsilon & 0 \\ \varepsilon & 0 & 0 \\ 0 & 0 & \dfrac{\varepsilon^2}{1-\varepsilon^2} \end{pmatrix},$$

where the matrices are representation of linear transformations with respect to the orthonormal cubic basis. By construction, the unperturbed crystal is in equilibrium with respect to these perturbations, and therefore the energy shows a quadratic dependence for small enough shears. Specifically, the energy as a function of ε has the simple form,

$$E_x^{\text{bcc}}(\varepsilon, V) = \hat{W}_0^{\alpha}(V) + C_x^{\text{bcc}}\varepsilon^2 + O(\varepsilon^4), \tag{8}$$

where $x = t$ or s denotes which shear. The C_x^{bcc} are combinations of the three independent bcc elastic constants; specifically,

$$C_t^{\text{bcc}} = C_{11} - C_{12}, \tag{9}$$

$$C_s^{\text{bcc}} = 2C_{44}. \tag{10}$$

The hcp phase requires the application of three volume conserving shears ($\boldsymbol{\varepsilon}_{t1}^{\text{hcp}}$, $\boldsymbol{\varepsilon}_{t2}^{\text{hcp}}$, and $\boldsymbol{\varepsilon}_{s}^{\text{hcp}}$) that are given by

$$\boldsymbol{\varepsilon}_{t1}^{\text{hcp}} = \begin{pmatrix} \varepsilon & 0 & 0 \\ 0 & -\varepsilon & 0 \\ 0 & 0 & \dfrac{\varepsilon^2}{1-\varepsilon^2} \end{pmatrix}, \quad \boldsymbol{\varepsilon}_{t2}^{\text{hcp}} = \begin{pmatrix} \dfrac{\varepsilon^2}{1-\varepsilon^2} & 0 & 0 \\ 0 & \varepsilon & 0 \\ 0 & 0 & -\varepsilon \end{pmatrix}, \quad \boldsymbol{\varepsilon}_{s}^{\text{hcp}} = \begin{pmatrix} 0 & 0 & \varepsilon \\ 0 & \dfrac{\varepsilon^2}{1-\varepsilon^2} & 0 \\ \varepsilon & 0 & 0 \end{pmatrix}.$$

These matrices represent linear transformations with respect to the lattice basis $\{[1\,0\,0\,0], [0\,1\,\bar{1}\,0], [0\,0\,0\,1]\}$ in standard hexagonal lattice notation.

Similar to the bcc phase, the energy as a function of ε for the hcp phase has the form

$$E_x^{\text{hcp}}(\varepsilon, V) = \hat{W}_0^{\alpha}(V) + C_x^{\text{hcp}}\varepsilon^2 + O(\varepsilon^3 \text{or } \varepsilon^4). \tag{11}$$

The last term is $O(\varepsilon^4)$ for $\boldsymbol{\varepsilon}_{t1}^{\text{hcp}}$ and $\boldsymbol{\varepsilon}_{t2}^{\text{hcp}}$; however, the final term is $O(\varepsilon^3)$ for $\boldsymbol{\varepsilon}_{s}^{\text{hcp}}$. Since very small ε's are used, both $O(\varepsilon^3)$ and $O(\varepsilon^4)$ are considered negligible. The C_x^{hcp} now are combinations of the five independent hcp elastic constants, namely,

$$C_{t1}^{\text{hcp}} = C_{11}(V) - C_{12}(V), \tag{12}$$

$$C_{t2}^{\text{hcp}} = \tfrac{1}{2}C_{11}(V) + \tfrac{1}{2}C_{33}(V) - C_{13}(V), \tag{13}$$

$$C_{s}^{\text{hcp}} = 2C_{44}(V). \tag{14}$$

In order to calculate the C_x^{bcc}'s and the C_x^{hcp}'s, the energy of the crystal is calculated with ε ranging from -0.05 to 0.05. Next, a polynomial is fit to this data, where the C_x^{bcc}'s and the C_x^{hcp}'s are determined by simple differentiation. The independent bcc elastic constants are found by simultaneously solving Eqs. (5), (9), and (10). Similarly, the independent hcp elastic constants are found by simultaneously solving Eqs. (6), (7), and (12)–(14). The calculated bcc and hcp elastic constants are shown in Fig. 5. At equilibrium (i.e., at zero pressure), the calculated bcc elastic constants are $C_{11} = 271\,\text{GPa}$, $C_{12} = 145\,\text{GPa}$, and $C_{44} = 101\,\text{GPa}$. The measured equilibrium bcc elastic constants

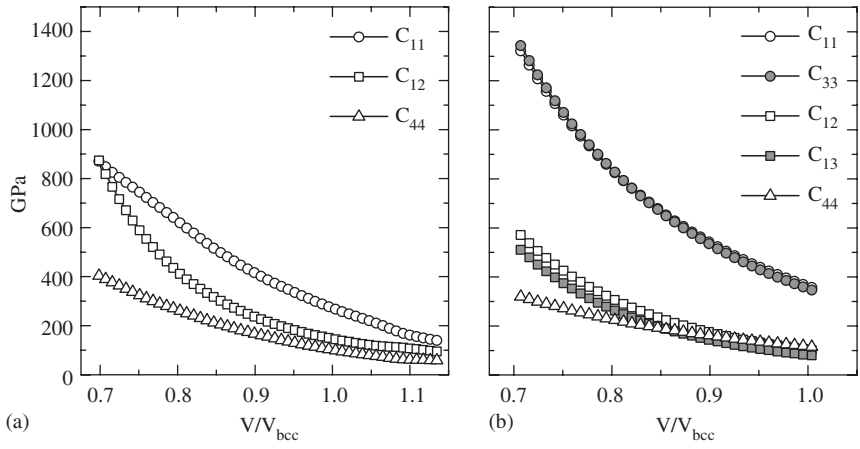

Fig. 5. DFT–GGA elastic constants of the bcc (a) and hcp (b) phases.

(Simmons and Wang, 1971) are $C_{11} = 243\,\mathrm{GPa}, C_{12} = 138\,\mathrm{GPa}$, and $C_{44} = 122\,\mathrm{GPa}$. Thus, our calculated bcc elastic constants compare reasonably well with experiments. Since hcp is not the ground state of Fe, there are no zero pressure experimental data to compare with. However, our calculated elastic constants do compare favorably with those calculated by Steinle-Neumann et al. (1999) utilizing the LAPW all-electron method. For both phases, the tensor of elastic constants is positive definite at all volumes in the computed range, and hence the resulting configurations are stable.

3. Microstructural optimization

A common model of microstructure development in materials with multi-well strain energy densities, such as (3), presumes that the microstructures of interest correspond to low-energy configurations, and that, consequently, their essential structure may be ascertained by investigating the absolute minimizers of the energy. However, energy functionals arising from strain energy densities as (3) often lack weak-sequential lower semi-continuity and their infimum is not attained in general (Dacorogna, 1989). The standard remedy is to introduce the quasiconvex envelope

$$QW(\mathbf{F}) = \frac{1}{|Q|} \inf_{\mathbf{u} \in W_0^{1,\infty}(Q)} \int_Q W(\mathbf{F} + D\mathbf{u})\,\mathrm{d}X, \tag{15}$$

where Q is the unit cube centered at 0, and $W_0^{1,\infty}(Q)$ denotes the space of functions whose distributional derivatives are essentially bounded and which vanish on ∂Q. Physically, $QW(\mathbf{F})$ represents the lowest energy density achievable by the material through the development of microstructure. The macroscopic deformations of a solid with reference configuration Ω are then identified with solutions of the relaxed problem

$$\inf_{\mathbf{y} \in \mathscr{X}} \left\{ \int_\Omega QW(D\mathbf{y})\,\mathrm{d}X \right\}, \tag{16}$$

where $\mathscr{X}$ is some suitable functional space, and $\mathbf{y}$ is the deformation mapping. For simplicity, the potential energy in (16) considers only imposed displacements on $\partial\Omega$. The defining property of problem (16) is that, under appropriate growth conditions for W, it does have a solution, and that this solution is the weak limit of minimizing sequences of the original problem.

The quasiconvex envelope QW of W therefore contains the *effective* constitutive behavior of microscopic regions of the material. However, no general algorithm for the determination of the quasiconvex envelope of an arbitrary energy density is known at present. A fallback strategy is to effect a partial relaxation of the energy density by recourse to *sequential lamination* (Kohn, 1991; Luskin, 1996), and the use of rank-1 convexification $RW(\mathbf{F})$ of $W(\mathbf{F})$ in lieu of $QW(\mathbf{F})$ in the macroscopic variational problem (16). We recall that the rank-1 convexification $RW(\mathbf{F})$ of $W(\mathbf{F})$ follows as the limit (Kohn and Strang, 1986, 1983)

$$RW(\mathbf{F}) = \lim_{k \to \infty} R_k W(\mathbf{F}), \tag{17}$$

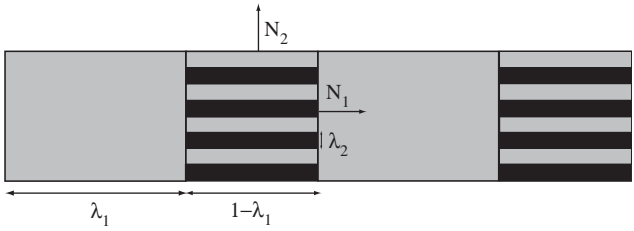

Fig. 6. Example of a rank-2 laminate; λ_1 and λ_2 are the volume fractions corresponding to levels 1 and 2, respectively, and $\mathbf{N}_1$ and $\mathbf{N}_2$ are the corresponding unit normals.

where $R_0 W(\mathbf{F}) = W(\mathbf{F})$ and $R_k W(\mathbf{F})$ is defined recursively as

$$R_k W(\mathbf{F}) = \inf_{\lambda,\mathbf{a},\mathbf{N}} \{(1-\lambda) R_{k-1} W(\mathbf{F} - \lambda \mathbf{a} \otimes \mathbf{N}) + \lambda R_{k-1} W(\mathbf{F} + (1-\lambda)\mathbf{a} \otimes \mathbf{N})\},$$
$$\lambda \in [0,1], \quad \mathbf{a}, \mathbf{N} \in \mathbb{R}^3, \quad |\mathbf{N}| = 1, \quad k \geqslant 1. \tag{18}$$

Here λ and $1-\lambda$ represent the volume fractions of the k-level variants, $\mathbf{N}$ is the unit normal to the planar interface between the variants and $\mathbf{a}$ is a vector, see Fig. 6.

Sequential lamination is, from a mathematical perspective, an imperfect solution to the absolute minimization of the functional in Eq. (16). However, laminated microstructures are ubiquitously found in nature. From this perspective, the nonlinear elasticity model and the search for absolute minimizers provide an imperfect description of the phenomenon. Rank-1 lamination has been found to be very successful at predicting microstructural features such as the variants involved in a laminate, their volume fractions and the habit plane, see e.g. Ball and James (1996). A sequential lamination algorithm consequently embeds information about the microstructure found in nature into the model; its use can be further advocated by including surface energy terms at the interfaces between variants.

A powerful additional reason for the adoption of a sequential lamination strategy is encountered when we numerically seek for minimizers of the unrelaxed problem, i.e., the problem in Eq. (16) with W instead of QW. The straightforward use of a finite element discretization of Ω leads to solutions that are strongly mesh-dependent and that display ubiquitous oscillations in the domain. The lamination algorithm we detail next gracefully sidesteps these difficulties.

3.1. Lamination algorithm

A practical algorithm for the exact computation of the rank-1 convexification of a general strain energy density in three dimensions is not known at present; in two dimensions a method is provided in Dolzmann (1999). Subsequently, we briefly review the sequential lamination algorithm introduced in Aubry et al. (2003) and refer the reader to the original source for further details. The aforementioned algorithm provides an approximation to the rank-1 envelope of a general strain energy density in three dimensions. We shall use this algorithm in the ensuing studies of the constitutive behavior of Fe.

Uniform deformations may be characterized as rank-0 laminates. A rank-1 laminate is a layered mixture of two deformation gradients, $\mathbf{F}^-$ and $\mathbf{F}^+$. Compatibility of deformations

then requires $\mathbf{F}^{\pm}$ to be rank-1 connected, i.e.,

$$\mathbf{F}^{+} - \mathbf{F}^{-} = \mathbf{a} \otimes \mathbf{N}, \tag{19}$$

where $\mathbf{a} \in \mathbb{R}^3$ and $\mathbf{N} \in \mathbb{R}^3$, $|\mathbf{N}| = 1$, is the normal to the interface between the two variants of deformation. The average deformation of the rank-1 laminate is

$$\mathbf{F} = \lambda^{+}\mathbf{F}^{+} + \lambda^{-}\mathbf{F}^{-}, \tag{20}$$

where $\lambda^{\pm} \in [0, 1]$ and $\lambda^{+} + \lambda^{-} = 1$. Recursively, a rank-$k$ laminate is a layered mixture of two rank-$(k-1)$ laminates, with average deformations $\mathbf{F}^{+}_{k-1}$ and $\mathbf{F}^{-}_{k-1}$, respectively, and such that $\mathbf{F}^{+}_{k-1}$ and $\mathbf{F}^{-}_{k-1}$ are compatible, i.e., satisfy Eq. (19) for some $\mathbf{a}_k$ and $\mathbf{N}_k$.

A rank-k laminate is more easily represented as the graph of a binary tree in which each node is the root of a rank-i laminate, $i \leqslant k$, and its two branches are roots for rank-$(i-1)$ laminates. It is perfectly possible to have the mass fraction λ at a node to be 0 or 1; this just indicates that instead of a layered mixture we have a homogeneous deformation at that node. An example of this representation is shown in Fig. 7. The missing leaves do not belong to the graph of this laminate.

A complete set of degrees of freedom for a rank-k laminate is obtained by considering the set of all mass fractions and vectors $\mathbf{a}$ and $\mathbf{N}$ at each branching node, in addition to the deformation at the root of the tree. Consequently, associated with each graph G of a sequential laminate there exists a set of degrees of freedom $\mathscr{J}_G$ that parametrize all possible microstructures with the same graph G.

Given a macroscopic deformation $\mathbf{F}$ and the graph G of a rank-k laminate, we seek the microstructure compatible with G having $\mathbf{F}$ as the deformation of the root node, such that the energy density $GW(\mathbf{F})$ of the laminate is infimized. In other words,

$$GW(\mathbf{F}) = \inf_{\mathscr{J}_G} \sum_i v_i W(\mathbf{F}_i), \tag{21}$$

where i runs over all leaves of G, $\mathbf{F}_i$ is the deformation of leaf i, and v_i is the volume fraction of the complete microstructure occupied by the variant in leaf i. The value of v_i is

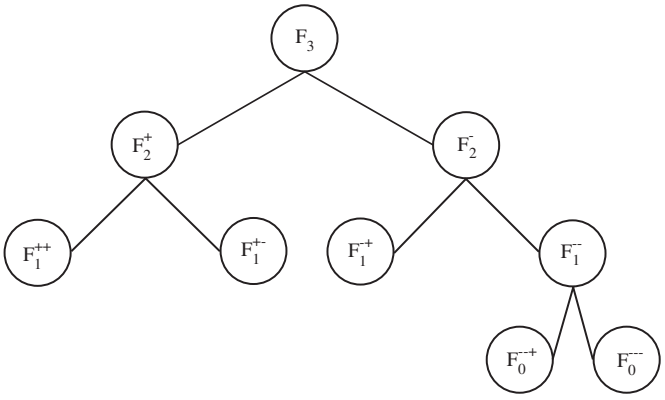

Fig. 7. Example: graph representation of a rank-4 laminate, in which some leaves are missing at the bottom of the tree. The mass fraction of these leaves is either 0 or 1, and therefore their deformation is equal to the average deformation of their parent node.

immediately obtained as the product of the mass fractions, the λ's, of all nodes above leaf i in the tree.

The rank-1 convexification follows by infimizing $GW(\mathbf{F})$ among all possible graphs, i.e.,

$$RW(\mathbf{F}) = \inf_{G} GW(\mathbf{F}). \tag{22}$$

It is clear that this problem exhibits combinatorial complexity as the rank of the test laminates increases, which makes a direct evaluation of (22) infeasible in general.

Alternatively, we adopt a local minimization criterion, in which we seek for a microstructure that is a minimizer under certain set of operations on the laminate. The algorithm can be easily described with a sequence of equilibration, pruning and branching steps. Given a macroscopic deformation $\mathbf{F}$, the algorithm is

(1) Set the graph G to be a single node, and let $\mathbf{F}$ be its deformation.
(2) Do until G does not change:
  (a) Equilibrate G, i.e., find $GW(\mathbf{F})$.
  (b) Prune from G all leaves with null mass fractions. Let G' be the resulting graph.
  (c) Compute the driving forces $f_i = W(\mathbf{F}_i) - R_1 W(\mathbf{F}_i)$ for every leaf i in G'.
  (d) Let $f_l = \max_i f_i$. If $f_l > 0$, branch leaf l in G'. Let the resulting graph be the new G.
(3) Compute $W_{\text{eff}}(\mathbf{F}) = GW(\mathbf{F})$, the effective strain energy density at $\mathbf{F}$.

The resulting microstructure is not necessarily the absolute minimizer of (22), but it is only a minimizer within $\mathscr{J}_G$ and with respect to certain topological changes in the graph of the laminate. For example, if a rank-2 laminate gives a lower energy configuration than the rank-0 one, but no rank-1 laminate has lower energy than the latter, the algorithm will not find it. This feature is similar to all global minimization problems; it is rather impossible to guarantee that a local minimum is an absolute minimizer for a general functional, unless further information is available. Also, to prevent some pathological minimizers of very large rank from appearing, a constant surface energy term with a nominal value of $1\,\mathrm{J/m^2}$ was included, following precisely the discussion and development in Aubry et al. (2003).

An undesired consequence of the local minimization is that $W_{\text{eff}}(\mathbf{F})$ may not be continuous with respect to $\mathbf{F}$ at rather isolated, and therefore rare, values of the macroscopic deformation. The algorithm can be modified to provide a continuous $W_{\text{eff}}(\mathbf{F})$ when $W(\mathbf{F})$ is, by fixing the topology of the laminate to the maximum graph of a rank-k laminate, and use it to find $GW(\mathbf{F})$. It comes at the expense of either severely restricting the rank of the resulting laminates or drastically increasing the computational cost of each lamination run.

4. Results

Next, we explore the behavior of iron through the phase transition in three different situations.

4.1. The effect of shear

As mentioned in the introduction, Section 1, shear has been postulated to play a key role in the mechanical behavior of Fe through the bcc–hcp phase transition. We quantify this

effect by applying a shear deformation $\boldsymbol{F}_s(\delta)$ on the boundary of the sample, and optimizing for the microstructure in the interior. Here $\boldsymbol{F}_s(\delta)$ consists of a linear compression from the reference, stress-free, bcc variant to a deformation at a smaller volume (V_f), simultaneous with a linearly increasing applied shear to a final shear ε_f. Specifically,

$$\boldsymbol{F}_s(\delta) = (1-\delta)\boldsymbol{I} + \delta \begin{pmatrix} \lambda & \varepsilon_f & 0 \\ \varepsilon_f & \lambda & 0 \\ 0 & 0 & \lambda \end{pmatrix}, \tag{23}$$

where δ ranges from 0 to 1 and λ is set such that $\det[\boldsymbol{F}_s(1)] = V_f/V_{bcc}$, where V_{bcc} is the atomic volume of the undeformed bcc phase.

We set V_f to $0.89V_{bcc}$, roughly the volume of the lowest attainable energy by the hcp phase, and found the evolution of the optimal microstructure as a function of δ for seven choices of ε_f; $\varepsilon_f = 0.00, 0.01, \ldots, 0.06$. Fig. 8 shows the predicted microstructure for three ε_f's over a range of volumes. We observe that the onset of microstructure, and hence the

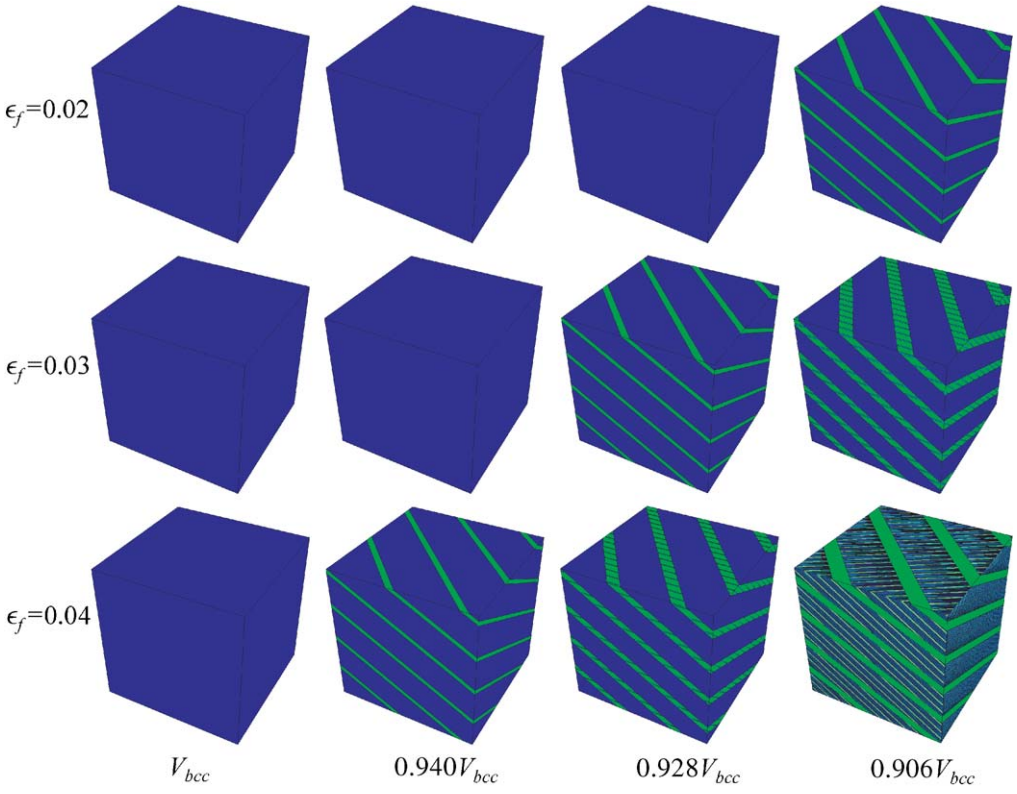

Fig. 8. The microstructure of Fe subject to $\boldsymbol{F}_s(\delta)$ (Eq. (23)) for three ε_f's (0.02, 0.03, and 0.04). The value of V_f/V_{bcc} for each column is 1.000, 0.940, 0.928, and 0.906 from left to right, respectively. Blue represents the bcc phase, while other colors represent specific hcp phases. All figures are plotted in the reference configuration.

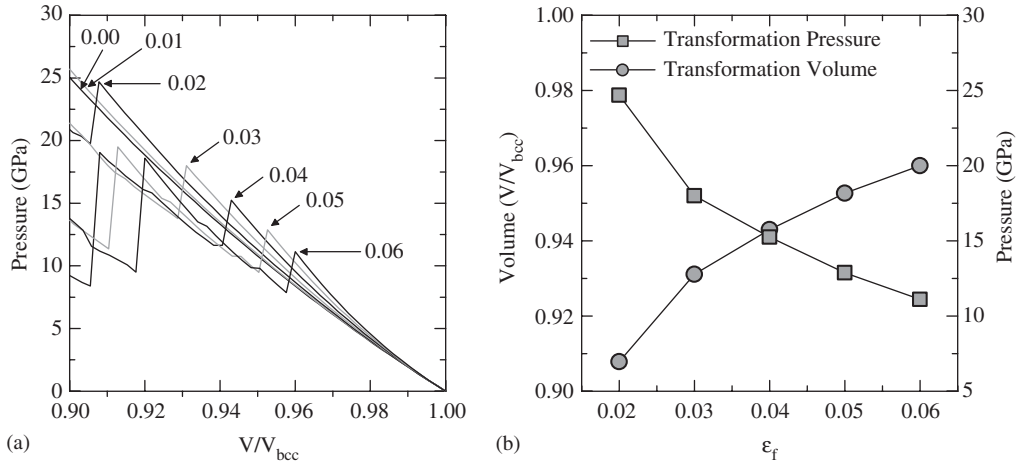

Fig. 9. The pressure/volume properties of Fe subject to $\boldsymbol{F}_s(\delta)$ (Eq. (23)) for seven ε_f's. (a) The pressure–volume plots for the seven ε_f's. The discontinuities indicate the onset of laminate microstructure, which is seen for $\varepsilon_f \geqslant 0.02$. Also, for $\varepsilon_f \geqslant 0.04$ and for $V/V_{bcc} \leqslant 0.92$ secondary discontinuities are observed that indicate additional lamination and the formation of more complex microstructure, as shown in Fig. 8. (b) The transformation pressure and volume as a function of ε_f, extracted from (a) as the pressure and volume immediately before the first discontinuity for $\varepsilon_f \geqslant 0.02$.

phase transformation, occurs at different volumes for different ε_f's. Moreover, at a specific volume, the complexity of the microstructure increases with ε_f; e.g., with $V = 0.906 V_{bcc}$ and $\varepsilon_f = 0.04$ we obtain a rank-4 laminate. Thus, this model predicts that the phase transformation characteristics (microstructure, onset, etc.) depend strongly on shear. We note that the lack of interfacial energy between phases prevents us from determining the length scale of the microstructure; this is the reason why no length scale is attached to Fig. 8. The quantitative predictions of the model are shown in Fig. 9, where we plot the pressure–volume relation for each ε_f (Fig. 9a) and the transformation pressure and volume as a function of ε_f (Fig. 9b). In Fig. 9a, the P–V discontinuities indicate the onset of lamination, i.e., the transformation onset. Deformations with ε_f's of 0.00 (i.e., hydrostatic compression) and 0.01 show no discontinuities. Thus, shear is required for the transformation to occur in this volume range. All ε_f's $\geqslant 0.02$ display at least one discontinuity. Additionally, ε_f's $\geqslant 0.04$ show secondary discontinuities for V/V_{bcc}'s $\leqslant 0.92$, indicating an increase in the complexity of the microstructure via additional lamination, as displayed for $\varepsilon_f = 0.04$ in Fig. 8. Fig. 9b shows the transformation pressure and volume as a function of ε_f, extracted from Fig. 9a as the pressure and volume immediately before the first discontinuity reached upon compression. The model predicts that the transformation volume increases toward V_{bcc} as the ε_f increases, i.e. less compression is required when more shear is applied. The transformation pressure is predicted to decrease from ≈ 25 GPa for $\varepsilon_f = 0.02$ to ≈ 11 GPa for $\varepsilon_f = 0.06$, which is in agreement with experimentally measured transformation pressures (Von Bargen and Boehler, 1990; Rueff et al., 1999; Huang et al., 1987). This demonstrates the sensitivity of the transformation pressure to relatively small shear deformations, and provides a feasible explanation to the observed dispersion of the experimental results.

4.2. Bulk transformation properties

Next we would like to explore the properties of Fe when fewer constraints are imposed on the boundary of the sample; for example by specifying the sample volume only. We seek to emulate experimental conditions with very compliant pressure exerting media. To this end, we apply the volume-conserving deformation $\boldsymbol{F}_M(V,\delta)$, which consists of a linear transformation from the low energy bcc deformation at a specific volume ($\boldsymbol{F}_{\mathrm{bcc}}(V)$) to a low energy hcp deformation at the same volume ($\boldsymbol{F}_{\mathrm{hcp}}(V)$). Specifically,

$$\boldsymbol{F}_M(V,\delta) = \beta[(1-\delta)\boldsymbol{F}_{\mathrm{bcc}}(V) + \delta\boldsymbol{F}_{\mathrm{hcp}}(V)]. \tag{24}$$

Here δ varies from 0 to 1. The low-energy deformation for the bcc phase over the volume range under consideration does not involve shear, therefore $\boldsymbol{F}_{\mathrm{bcc}} = (V/V_{\mathrm{bcc}})^{1/3}\boldsymbol{I}$. We choose $\boldsymbol{F}_{\mathrm{hcp}}(V)$ to coincide with the continuous compression of $\mathbf{U}^1$, $\boldsymbol{F}_{\mathrm{hcp}}(V) = \sqrt{\mathbf{C}^1(V)}$. Alternatively, any $\boldsymbol{U}^\alpha$ from Table 1 would result in a symmetrically identical $\boldsymbol{F}_M(V,\delta)$. Finally, β is a small volume-conserving factor, where β is chosen such that $\det \boldsymbol{F}_M(V,\delta) = V/V_{\mathrm{bcc}}$. We apply $\boldsymbol{F}_M(V,\delta)$ over a V/V_{bcc} range from 0.86 to 1.02, where the δ that minimizes the energy for a V/V_{bcc} gives the properties of Fe at that V/V_{bcc}. We therefore explore the properties of Fe under some sort of less constrained boundary conditions.

Fig. 10 gives the energy (E), pressure (P), and fraction of the hcp phase (χ_{hcp}) for the volume range $0.86 \leqslant V/V_{\mathrm{bcc}} \leqslant 1.02$. In Fig. 10c, we observe that for $V/V_{\mathrm{bcc}} \geqslant 0.95$ and for $V/V_{\mathrm{bcc}} \leqslant 0.88$ our model predicts that Fe will consist of pure crystalline bcc and hcp, respectively. However, for $0.88 < V/V_{\mathrm{bcc}} < 0.95$, the lowest energy phase is predicted to be a laminate microstructure of the two phases, where we term this region the "transformation region". The transformation region is slightly smaller but similar to the one predicted by the Gibbs construction (GC), since our model predicts pure bcc and hcp phases to exist at lower and higher volumes, respectively. For completeness, we show the GC predictions with thick dashed black lines in all three plots of Fig. 10. Both our model

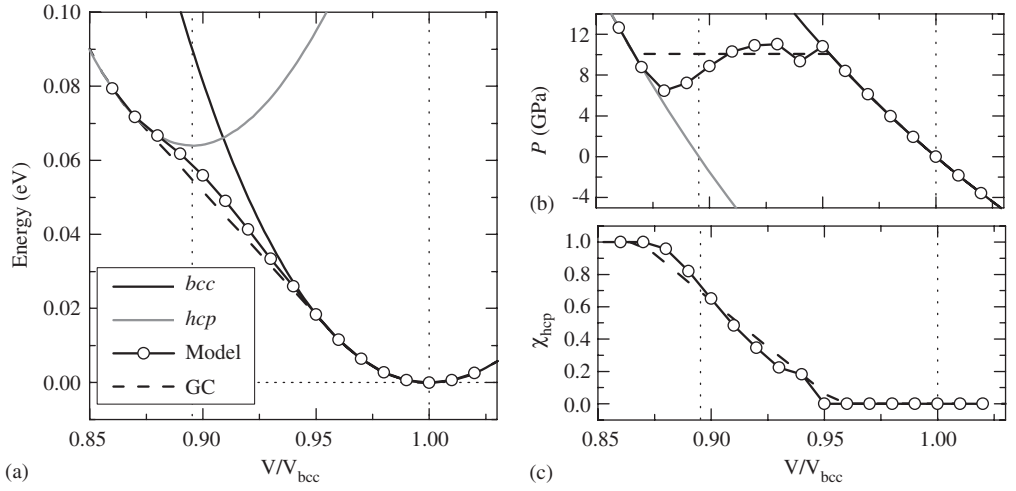

Fig. 10. The (a) energy, (b) pressure, and (c) fraction of the hcp phase χ_{hcp} as a function of atomic volume.

and the GC predict that the transformation to the pure hcp phase occurs at V's less than the equilibrium hcp volume, which is simply a consequence of the energy difference of the two phases. In Fig. 10a, the energy is shown to vary smoothly and monotonically throughout the volume range considered. Additionally, the energy is lower than the pure phases in the transformation region, indicating that the laminated microstructure is more stable than the pure phases. This result is similar to the prediction of the GC; however, we observe a slight deviation from the GC, with a slight upward bowing of the energy. Fig. 10b shows that our model predicts a bcc $\rightarrow$ hcp TP upon loading (decreasing V) of ≈ 10.2 GPa, which is similar to the GC prediction of 10 GPa. However, our model also predicts that the pressure varies in the transformation region, which the GC does not account for. This pressure variation is a consequence of the energy bowing observed in Fig. 10a and results in a pressure hysteresis. Specifically, in a pressure-controlled experiment, the bcc $\rightarrow$ hcp transformation onsets at ≈ 10.2 GPa, while upon unloading (increasing V) we predict a hcp $\rightarrow$ bcc transformation pressure of ≈ 5 GPa. Thus, our model predicts a hysteresis width in the transformation pressure of ≈ 5.2 GPa. As mentioned in the introduction, it has been suggested that the pressure width of this hysteretic loop is correlated with the compliance of the pressure exerting medium. In our particular case, with the proposed relaxation of the constraints on the boundary we found a pressure width consistent with the experimentally measured width of 6.2 GPa by Taylor et al. (1991a).

The deviations from the GC described above—the smaller transformation region, the energy bowing, and the pressure hysteresis—can be attributed to the Hadamard compatibility condition; i.e., the interface between neighboring deformations must not result in any slip or gaps in the material. In order to further analyze the consequences of this condition, we must first define some quantities. Let $\boldsymbol{F}_\alpha(V)$ and $\boldsymbol{F}_\omega(V)$ be the minimum energy deformations of two phases (α and ω) that can undergo a pressure-driven martensitic transformation. These two deformations are not compatible in general, therefore, let $\boldsymbol{F}_{\omega^*}(V)$ and $\boldsymbol{F}_{\alpha^*}(V)$ be the lowest-energy deformations of the ω and α phases that are compatible with $\boldsymbol{F}_\alpha(V)$ and $\boldsymbol{F}_\omega(V)$, respectively. Finally, let $V_{x\rightarrow y}$ be the volume at which the GC gives the beginning of the $x \rightarrow y$ transformation.

Using the above definitions and Fig. 11, we can now give a simple description of consequences of the Hadamard compatibility condition. Consider compression of the pure α phase. At the point in compression when $V = V_{\alpha\rightarrow\omega}$, the GC states that mixing the phases is energetically favorable. However, $\boldsymbol{F}_\alpha(V_{\alpha\rightarrow\omega})$ and $\boldsymbol{F}_\omega(V_{\omega\rightarrow\alpha})$ are not compatible, therefore the transformation cannot begin. Upon further compression, the transformation begins when $V = V_{\alpha\rightarrow\omega^*}$ because $\boldsymbol{F}_\alpha(V_{\alpha\rightarrow\omega^*})$ and $\boldsymbol{F}_{\omega^*}(V_{\omega^*\rightarrow\alpha})$ are compatible. By construction, the line of common tangent given by the GC has a steeper slope for the $\alpha \rightarrow \omega^*$ transformation than for the $\alpha \rightarrow \omega$ transformation and therefore the transformation pressure is larger. Considering the decompression of the pure ω phase results in similar behavior. At the point during the expansion of ω when $V = V_{\omega\rightarrow\alpha}$ the GC states that it is energetically favorable to mix the α and ω phases. As stated above,$\boldsymbol{F}_\alpha(V_{\alpha\rightarrow\omega})$ and $\boldsymbol{F}_\omega(V_{\omega\rightarrow\alpha})$ are not compatible, therefore, the transformation cannot begin. It is not until $V_{\omega\rightarrow\alpha^*}$ that the transformation begins, however it begins as the $\omega \rightarrow \alpha^*$ transformation. By construction, the slope of the line of common tangent for the $\omega \rightarrow \alpha^*$ is less steep than that of the $\omega \rightarrow \alpha$ transformation, therefore, the transformation pressure will be decreased. Thus, this simple argument outlining consequences of the Hadamard compatibility condition can explain the decrease in the size of the

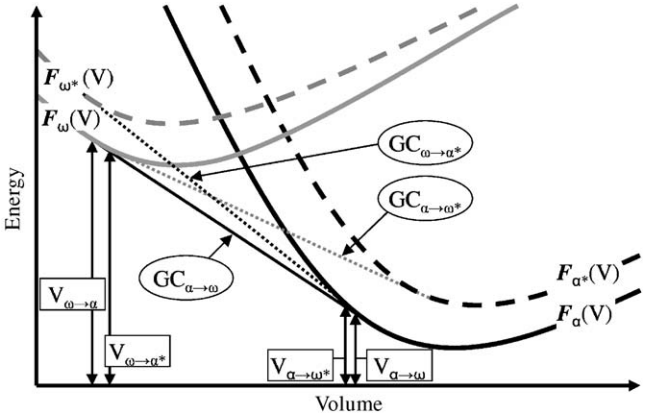

Fig. 11. A schematic explanation of the consequences of the Hadamard compatibility condition, namely, the observed energy bowing and pressure hysteresis. The solid gray and black lines represent the equations of state of two phases that undergo a martensitic phase transformation (in our case the bcc and hcp phases of Fe), where the thin black line represents the prediction from the Gibbs construction. The thick dashed gray and black lines represent the equations of state of the phases subject to a small deformation, where the dotted gray and black lines represent the prediction of the Gibbs construction between the deformed and undeformed phases.

transformation region, the energy bowing, and the pressure hysteresis. We believe that this is true not only for the bcc ↔ hcp transformation in Fe, but it should be true for all pressure-driven martensitic transformations that produce a mixed phase laminate microstructure.

4.3. Directional deformation

Under shock-loading conditions, materials undergo compressions that are not hydrostatic, but rather are uniaxial compressions along the direction of shock wave propagation. Since the crystals are not isotropic, the direction of the compression should affect the transformation properties. In order to investigate the directional dependence of the bcc–hcp transformation upon uniaxial compression, we apply a series of uniaxial compressions that span all symmetry-independent directions within the bcc unit cell.

We define a vector $\hat{\tau} = \langle xyz \rangle$ in the reference frame of the cubic bcc two-atom unit cell (i.e., in the reference frame of $\boldsymbol{U}^0$, the identity). A deformation of a uniaxial compression along $\hat{\tau}$ is given by

$$\boldsymbol{F}(\hat{\tau}, v) = v\hat{\tau} \otimes \hat{\tau} + \hat{\tau}' \otimes \hat{\tau}' + \hat{\tau}'' \otimes \hat{\tau}'', \tag{25}$$

where $\hat{\tau}'$ and $\hat{\tau}''$ are arbitrary vectors constructed such that $\hat{\tau}$, $\hat{\tau}'$ and $\hat{\tau}''$ are mutually orthogonal. The quantity v controls the amount of compression, where $v = \det \boldsymbol{F}(\hat{\tau}, v)$. Therefore, $\boldsymbol{F}(\hat{\tau}, v) = \boldsymbol{I}$ for $v = 1$, i.e. no compression. However, for $v < 1$ Eq. (25) gives a deformation of a compression along $\hat{\tau}$ to a fractional volume v. We therefore investigate a series of $\hat{\tau}$'s that span all symmetry independent directions within the bcc unit cell. In the bcc crystal, all symmetry-independent directions are included in the family of vectors $\hat{\tau} = \langle 1yz \rangle$, where y and z range from 0 to 1.

Fig. 12 displays the volume (given by v) and pressure of the bcc crystal immediately before the transformation onset for all possible directional deformations $\hat{\tau} = \langle 1yz \rangle$. We

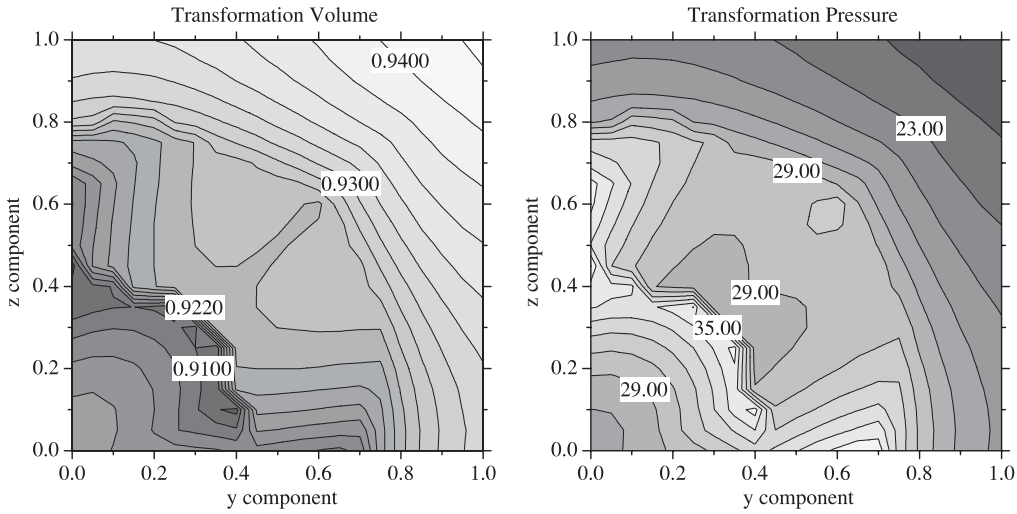

Fig. 12. The transformation volume (in units of V/V_{bcc}) and pressure (in units of GPa) for compression parallel to the vector $\langle 1yz\rangle$. The difference between contour lines is 0.002 V/V_{bcc} and 1.5 GPa for the transformation volume and pressure plots, respectively.

observe the expected symmetry about the $y = z$ line. The transformation pressure for all $\hat{\tau}$'s is >20 GPa, suggesting that during uniaxial compression insufficient shear is present to facilitate the transformation at low pressures. The highest transformation pressure ($\sim$38 GPa) and lowest transformation volume ($\sim 0.91\,\mathrm{V/V_{bcc}}$) is given by $\sqrt{y^2+z^2} \approx 0.4$. The directions of lowest transformation pressure are $\langle\sim 1\sim 0\sim 0\rangle$, $\langle\sim 1\sim 1z\rangle$, and $\langle\sim 1y\sim 1\rangle$. Specifically, the transformation pressures for the simple axes $\langle 1\,0\,0\rangle$, $\langle 1\,1\,0\rangle$, and $\langle 1\,1\,1\rangle$ are 26.94, 25.61, 20.10 GPa, respectively. The fact that compression along the simple axes facilitates the transformation is a consequence of the transformation path. Since the shear needed to transform bcc–hcp involves directional deformations along $\langle 1\,0\,0\rangle$ and $\langle 1\,1\,0\rangle$ directions (Fig. 1), it is perhaps not surprising that compression along these axes, and along the $\langle 1\,1\,1\rangle$ (which is a combination of the $\langle 1\,0\,0\rangle$ and $\langle 0\,1\,1\rangle$ directions), decreases the transformation pressure.

5. Conclusions

In summary, we created a path for the construction of ab initio-based nonlinear elastic energy densities, applied it to the bcc and hcp phases of Fe, and used the energetic landscape to explore some properties of the bcc-to-hcp transformation.

Perhaps the most appealing aspect of the proposed method to construct energetic landscapes from ab initio is its simplicity and generality. More sophisticated approaches to the construction of nonlinear elastic energy densities using polynomial bases with proper invariance properties have been proposed (see, e.g., Smith and Rivlin, 1958; Zimmer, 2004). Nevertheless, it remains to be seen whether they can be appropriately combined with the wealth of information extracted from quantum mechanics; these have mostly been used to build appropriate elastic energy density functions that match the elastic moduli at specific transformation strains.

The kinematic reduction proposed herein to describe transformations from bcc to hcp is useful, but not fully satisfactory. A more elegant solution is likely to exists by considering a super bcc unit cell with a large number of shuffles. The resulting severe increase in complexity would provide a clean path to consider an arbitrary number of variants; notwithstanding the associated analysis may be very involved, for a complete characterization of symmetries of *nonessential* descriptions is not readily available.

We have used this model to explore properties of the bcc–hcp transformation in Fe. We investigated the role of shear by applying a linear compression from the zero stress bcc deformation to a deformation at a lower volume with a specified final shear (Eq. (23)). Our model displays a strong dependence on the final shear specified (Figs. 8 and 9). In particular, for the extent of compression we consider, no transformation is predicted for nearly hydrostatic compression ($\varepsilon_f = 0.00$ and 0.01). Also, the model predicts a transformation pressure range of 25–10 GPa for a final shear range of 0.02–0.06, suggesting that the compliance of the pressure exerting medium in experiments aimed at measuring the onset of the transition may critically determine their outcome, as hypothesized in Von Bargen and Boehler (1990).

We have also predicted the average bulk properties of Fe by applying a volume-conserving linear transformation from bcc to hcp (Eq. (24)) at specific volumes (Fig. 10). Our model predicts bulk properties of Fe that are somewhat similar to that of the Gibbs construction, where lamination (phase mixing) lowers the energy of the system. However, our model significantly deviates from the Gibbs construction, where we observe a slightly smaller transformation region and an upward bowing of the energy. The energy bowing produces a loading–unloading pressure hysteresis of 5.2 GPa, which is similar to the measured hysteresis width by some authors. We attribute this energy bowing, and subsequent pressure hysteresis, to the Hadamard compatibility condition (Fig. 11) that forces kinematic compatibility on the microstructure. Specifically, laminates do not consist of a mixture of low energy bcc and hcp deformations, but rather a mixture with at least one higher energy bcc and hcp deformation.

We have also investigated the transformation properties of Fe under uniaxial compression (Eq. (25)) along different directions (Fig. 12). We predict high transformation pressures (38 GPa > TP > 20 GPa) for all directions, which is likely due to insufficient shear during compression. The lowest transformation pressures were predicted for directions nearly parallel to $\langle 1\,0\,0\rangle$ axes and $\{1\,1\,0\}$ planes, which is consistent with the transformation mechanism. This results suggest that a more complex deformation pattern may be present in shock-loaded samples; for example, suitable oriented grains may compress in the direction of the shock and expand transversally to it, allowing the transformation to occur at the observed lower pressures.

We close by pointing out the strengths and limitations of our model. Since all input to this model was derived from first-principles calculations, this approach may be considered to be predictive. Moreover, the variant energy function we employ (Eq. (4)) allows us to add more (or less) variants, or increase the volume range of preexisting variants, by performing more DFT calculations, if deemed necessary. The nature of this model also allows us to simulate structures on the micron scale, which is too large for current molecular dynamics simulations. Also, our model is not limited to purely volumetric deformation; it can account for any arbitrary deformation.

Lastly, we point out some quantities not yet accounted for in the model. First, the model does not yet have physically derived interfacial energies, therefore the thickness of the

laminates is arbitrary. Second, since we generate the model input using DFT, the model is inherently at 0 K. Third, the model does not contain fcc variants, which could be important during the transformation. Finally, the energy function we consider is purely elastic, however, plasticity may affect the transformation by directly contributing to the energy or loosening the restrictions of the Hadamard compatibility condition. Most, if not all, of these effects can and will be included in future work.

Acknowledgements

We gratefully acknowledge support through Caltech's DOE ASCI/ASAP Center for the Simulation for the Dynamic Response of Materials and from the Office of Naval Research. We also acknowledge Dr. Matt Fago, whose implementation of the lamination algorithm of (Aubry et al., 2003) is employed in this work.

References

Ashcroft, N., Mermin, N., 1976. Solid State Physics. Saunders College Publishers.

Aubry, S., Fago, M., Ortiz, M., 2003. A constrained sequential-lamination algorithm for the simulation of sub-grid microstructure in martensitic materials. Comput. Method Appl. Math. 192, 2823–2843.

Ball, J., James, R.D., 1996. Fine phase mixtures as minimizers of energy. Z. Angew. Math. Mech. 76, 13–52.

Bancroft, D., Peterson, E., Minshall, S., 1956. Polymorphism of iron at high pressure. J. Appl. Phys. 27 (3), 291–298.

Barker, L., Hollenbach, R., 1974. Shock wave study of the $\alpha \leftrightarrow \varepsilon$ phase transition in iron. J. Appl. Phys. 45 (11), 4872–4887.

Bhattacharya, K., 2003. Microstructure of Martensite: Why it Forms and How it Gives Rise to the Shape-Memory Effect. Oxford University Press, Oxford, UK.

Bhattacharya, K., Conti, S., Zanzotto, G., Zimmer, J., 2004. Crystal symmetry and the reversibility of martensitic transformations. Nature 428, 55–59.

Blöchl, P., 1994. Projector augmented-wave method. Phys. Rev. B 50 (24), 17953–17979.

Bundy, F., 1965. Pressure–temperature phase diagram of iron to 200 kbar, 900 °C. J. Appl. Phys. 36 (2), 616–620.

Burgers, W., 1934. On the process of transition of the cubic-body-centered modification into the hexagonal-close-packed modification of zirconium. Physica 1, 561–586.

Caspersen, K., Lew, A., Ortiz, M., Carter, A., 2004. Importance of shear in the bcc-to-hcp transformation in iron. Phys. Rev. Lett. 93, 115501.

Chen, Y., Ho, K.M., Harmon, B., 1988. First-principles study of the pressure-induced bcc–hcp transition in B. Phys. Rev. B 37, 283.

Cohen, R., Stixrude, L., Wasserman, E., 1997. Tight-binding computations of elastic anistropy of Fe, Xe, and Si under compression. Phys. Rev. B 56 (14), 8575–8589.

Dacorogna, B., 1989. Direct Methods in the Calculus of Variations. Springer, Berlin.

Dolzmann, G., 1999. Numerical computation of rank-one convex envelopes. SIAM J. Numer. Anal. 36 (5), 1621–1635.

Ekman, M., Sadigh, B., Einarsdotter, K., Blaha, P., 1998. Ab initio study of the martensitic bcc–hcp transformation in iron. Phys. Rev. B 58 (9), 5296–5304.

Ericksen, J., 1970. Nonlinear elasticity of diatomic crystals. Int. J. Solids Struct. 6, 951–957.

Ericksen, J., 1984. The Cauchy and Born hypothesis for crystals. In: Gurtin, M. (Ed.), Phase Transformations and Material Instabilities in Solids. Academic Press, New York, pp. 61–77.

Ericksen, J., 1997. Equilibrium theory for X-rays observations. Arch. Ration. Mech. Anal. 139, 181–200.

Ericksen, J., 1999. On groups occurring in the theory of crystal multi-lattices. Arch. Ration. Mech. Anal. 148, 145–178.

Fago, M., Hayes, R., Carter, E., Ortiz, M., 2004. Density-functional-theory-based local quasicontinuum method: prediction of dislocation nucleation. Phys. Rev. B 70 (10), 100102(4).

Fonseca, I., 1987. Variational methods for elastic crystals. Arch. Ration. Mech. Anal. 97, 189–220.

Giles, P., Logenbach, M., Marder, A., 1971. High-pressure $\alpha \leftrightarrow \varepsilon$ martensitic transformation in iron. 42(11), 4290–4295.

Gornostyrev, Y.N., Katsnel'son, M.I., Kuznetsov, A.R., Trefilov, A.V., 1999. Microscopic description of the kinetics of a martensitic transition in real crystals: bcc–hcp transition in Zr. JETP Lett. 70 (6), 380–384.

Huang, E., Bassett, W., Tao, P., 1987. Pressure–temperature–volume relationship for hexagonal close packed iron determined by synchrotron radiation. J. Geophys. Res. 92 (B8), 8129–8135.

Johnson, P., Stein, B., Davis, R., 1962. Temperature dependence of shock-induced phase transformations in iron. J. Appl. Phys. 33 (2), 557–561.

Kadau, K., Germann, T., Lomdahl, P., Holian, B., 2002. Microscopic view of structural phase transitions induced by shock waves. Science 296, 1681–1684.

Knittle, E., 1995. Static compression measurements of equations of state. In: Ahrens, T. (Ed.), Mineral Physics and Crystallography: A Handbook of Physical Constants. American Geophysical Union Press, pp. 184–209.

Kohn, R., 1991. Relaxation of a double-well energy. Continuum Mech. Thermodyn. 3, 193–236.

Kohn, R., Strang, G., 1983. Explicit relaxation of a variational problem in optimal-design. Bull. Am. Math. Soc. 9 (2), 211–214.

Kohn, R., Strang, G., 1986. Optimal design and relaxation of variational problems i–ii–iii. Commun. Pure Appl. Math. 39, 113–137, 139–182, 353–377.

Kohn, W., Sham, L., 1965. Self-consistent equations including exchange and correlation effects. Phys. Rev. 134, 737–741.

Kresse, G., Furthmüller, J., 1996. Efficient iterative schemes for ab initio total-energy calculations using a plane-wave basis set. Phys. Rev. B 54, 11169–11186.

Kuznetsov, A.R., Gornostyrev, Y.N., Katsnelson, M.I., Trefilov, A.V., 2001. Effect of the dislocations on the kinetics of a martensitic transition and simulation of bcc–hcp transformation in Zr. Mat. Sci. Eng. A A309–310, 168–172.

Luskin, M., 1996. On the computation of crystalline microstructure. Acta Numerica 5, 191–257.

Mao, H., Bassett, W., Takahashi, T., 1967. Effect of pressure on crystal structure and lattice parameters of iron up to 300 kbar. J. Appl. Phys. 38 (1), 272–276.

Marsden, J., Hughes, T., 1994. Mathematical Foundations of Elasticity. Dover, New York.

Monkhorst, H., Pack, J., 1976. Special points for brillouin-zone integrations. Phys. Rev. B 13, 5188–5192.

Moroni, E., Jarlborg, T., 1996. Bcc and hcp phase competition in Fe. Europhys. Lett. 33 (3), 223–228.

Morris, J., Ho, K., 2001. Molecular dynamic simulation of a homogeneous bcc–hcp transition. Phys. Rev. B 63, 224116.

Perdew, J.P., Chevary, J.A., Vosko, S.H., Jackson, K.A., Pederson, M.R., Singh, D.J., Fiolhais, C., 1992. Atoms, molecules, solids, and surfaces: applications of the generalized gradient approximation for exchange and correlation. Phys. Rev. B 46 (11), 6671–6687.

Pitteri, M., 1985. On $v+1$-lattices. J. Elasticity 15, 3–25.

Pitteri, M., Zanzotto, G., 2003. Continuum Models for Phase Transitions and Twinning in Crystals. Chapman & Hall, CRC, New York, Boca Raton, FL.

Rueff, J.P., Krisch, M., Cai, Y.Q., Kaprolat, A., Hanfland, M., Lorenzen, M., Masciovecchio, C., Verbeni, R., Sette, F., 1999. Magnetic and structural α–ε phase transition in Fe monitored by X-ray emission spectroscopy. Phys. Rev. B 60 (21), 14510–14512.

Simmons, G., Wang, H., 1971. Single Crystal Elastic Constants and Calculated Aggregate Properties: A Handbook. MIT Press, Cambridge, MA.

Smith, G., Rivlin, R., 1958. The strain-energy function for anisotropic elastic materials. Trans. Am. Math. Soc. 88, 175–193.

Söderlind, P., Moriarty, J., Wills, J., 1995. First-principle theory of iron up to earth-core pressures: structural, vibrational, and elastic properties. Phys. Rev. B 53, 14063–14072.

Steinle-Neumann, G., Stixrude, L., Cohen, R., 1999. First-principles elastic constants for the hcp transition metals Fe, Co, and Re at high pressure. Phys. Rev. B 60 (2), 791–799.

Stixrude, L., Cohen, R., Singh, D., 1994. Iron at high pressure: linearized-augmented-plane-wave computations in the generalized-gradient approximation. Phys. Rev. B 50 (9), 6442–6445.

Taylor, R., Pasternak, M., Jeanioz, R., 1991a. Hysteresis in the height pressure transformation of bcc-to-hcp-iron. J. Appl. Phys. 69 (8), 6126–6128.

Taylor, R., Pasternak, M., Jeanloz, R., 1991b. Hysteresis in the high pressure transformation of bcc-to-hcp iron. J. Appl. Phys. 69 (8), 6126–6128.

Vočadlo, L., et al., 1997. First principles calculations on crystalline and liquid iron of earth's core conditions. Faraday Discuss. 106, 205–217.

Von Bargen, N., Boehler, R., 1990. Effect of non-hydrostaticity on the α–ε transition of iron. High Pressure Res. 6, 133–140.

Zimmer, J., 2004. Stored energy functions for phase transitions in crystals. Arch. Ration. Mech. Anal. 172, 191–212.